ELSEVIER

Contents lists available at ScienceDirect

Advances in Water Resources

journal homepage: www.elsevier.com/locate/advwatres





Advancing Characterization and Modeling of Space-Time Correlation Structure and Marginal Distribution of Short-Duration Precipitation

Giuseppe Mascaro a,*, Simon Michael Papalexiou b, Daniel B. Wright c

- a School of Sustainable Engineering and the Built Environment, Arizona State University, Tempe, AZ, USA
- ^b Civil Engineering, University of Calgary, Calgary, Canada
- ^c Civil and Environmental Engineering, University of Wisconsin-Madison, Madison, WI, USA

ARTICLE INFO

Keywords:

Short-duration precipitation Multisite stochastic rainfall modeling Space-time rainfall correlation Rainfall probability distributions

ABSTRACT

The statistical characterization of precipitation (P) at short durations (\leq 24 h) is crucial for practical and scientific applications. Here, we advance the knowledge of and ability to model the space-time correlation structure (STCS) and marginal distribution of short-duration P using a network of rain gages in central Arizona with one of the largest densities and spatial coverages in the world. We separately analyze summer and winter P sampled at multiple durations, Δt , from 0.5 to 24 h. We first identify an analytical model and a three-parameter distribution that robustly capture the empirical STCS and marginal distribution of P, respectively, across Δt 's. We then conduct Monte Carlo experiments consisting of multisite stochastic simulations of P time series to explore the spatial and seasonal variability of these properties. Significant seasonal differences emerge, especially at low Δt . Summer (winter) P exhibits weak (strong) correlation structure and heavy- (light-)tailed distributions resulting from short-lived, isolated thunderstorms (widespread, long-lasting frontal systems). The STCS of P is most likely homogeneous and isotropic except for winter at $\Delta t \geq 3$ h, where anisotropy could be introduced via the motion of frontal storms. The spatial variability of the marginal distribution is reproduced by a regional parameterization dependent on elevation in all cases except, again, for winter at $\Delta t \geq 3$ h where additional factors are needed to explain the variability of the mean P intensity. This work provides insights to improve stochastic P models and validate convection-permitting models used to investigate the mechanisms driving changes in short-duration P.

1. Introduction

Quantifying the spatiotemporal variability of precipitation (P) at short durations (here, ≤24 h) is crucial for several practical and scientific goals. It is key to generate more realistic design storms for urban stormwater infrastructure (Gires et al. 2014; Ichiba et al. 2018; Peleg et al. 2013), improve estimates of areal reduction factors used to convert extreme point P into areal averaged P (Wright et al. 2013; Veneziano and Langousis 2005), and increase the accuracy and resolution of indirect P estimates from weather radars (Krajewski et al. 2010) and satellite sensors (Tang et al. 2016). The knowledge of short-duration P variability is also needed to develop and test stochastic models of temporal, spatial, and spatiotemporal P fields (Venugopal et al. 1999; Schertzer and Lovejoy 1987; Deidda 2000; Bárdossy and Pegram 2009; Burton et al. 2008; Papalexiou and Serinaldi 2020; Papalexiou 2018; Papalexiou et al. 2021; Paschalis et al. 2013; Peleg et al. 2017; Kim and Onof 2020;

Rebora et al. 2006; among others). The high-resolution P time series or grids generated by these models have been useful to increase the value of physics-based distributed hydrologic models in studies on flood-generating mechanisms (Paschalis et al. 2014; Mascaro et al. 2013b), flood frequency (Wright et al. 2014), and climate change impacts (Piras et al. 2014), among other goals. Moreover, outputs of space-time P models have the potential to enhance the accuracy of P forecast (Harris et al. 2001) and, in turn, the skill of flood and flash flood forecasting systems (Seo et al. 2013; Alfieri and Thielen 2015), particularly in urban regions where watersheds have short response times (Hjelmstad et al. 2021).

Many studies have provided insights into the spatiotemporal variability of short-duration P by investigating the presence of scaling regimes (i.e., time and/or space intervals where the P statistical properties are linked via power law relations) across a wide range of temporal and spatial scales through spectral, multifractal, and wavelet-based

E-mail address: gmascaro@asu.edu (G. Mascaro).

^{*} Corresponding author: Giuseppe Mascaro, School of Sustainable Engineering and the Built Environment, Arizona State University, 777 E. University Dr., Tempe, AZ 85287

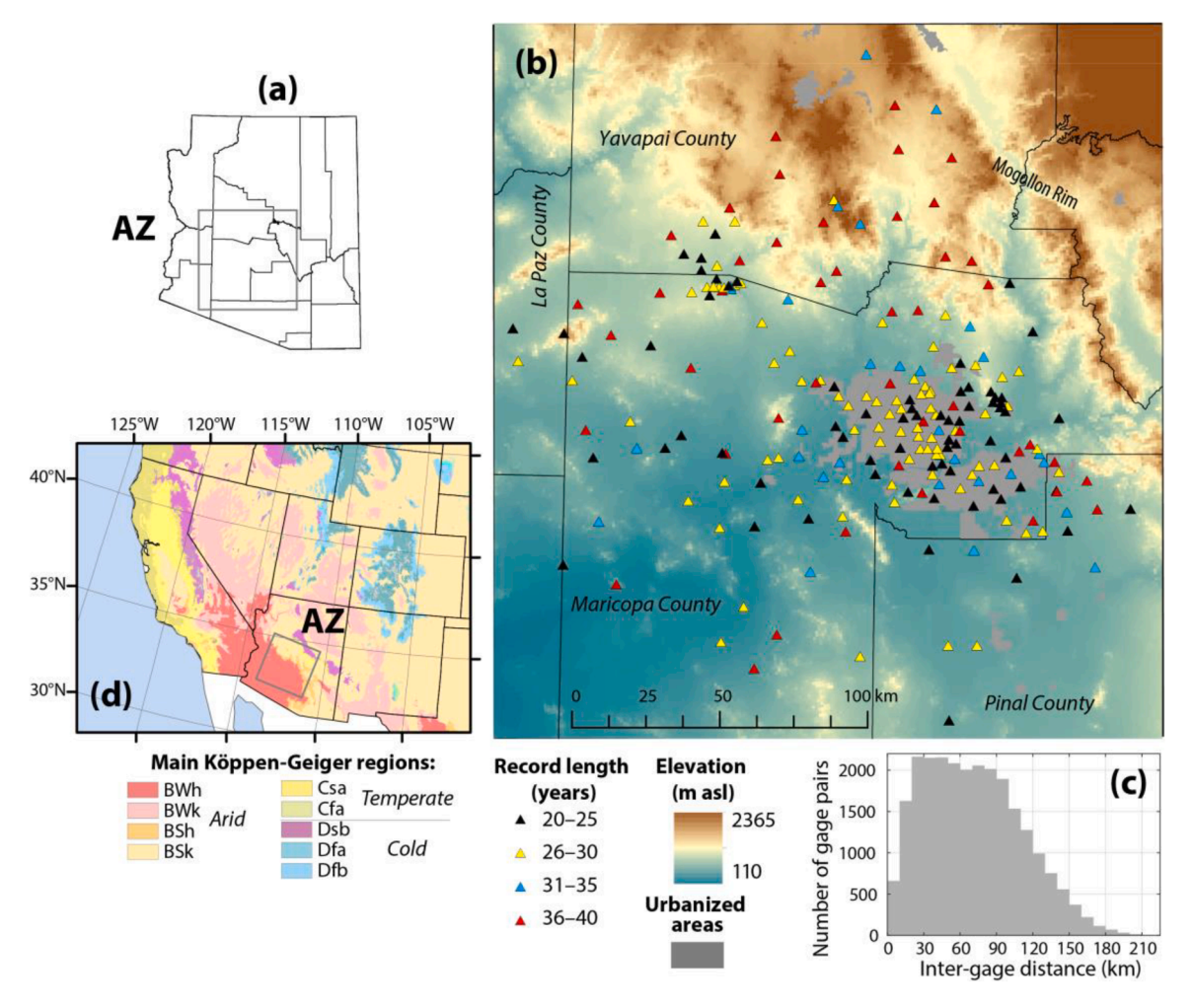


Fig. 1. (a) Study area in central Arizona (AZ) within the county boundaries. (b) Digital elevation model (derived from the U.S. Geological Survey National Elevation Dataset) of the study region in the Maricopa, La Paz, Yavapai, and Pinal Counties along with the location of the rain gages of the FCDMC network, color-coded based on the corresponding record length. Urbanized areas are also shown. (c) Frequency distribution of the inter-gage distance. (d) Köppen-Geiger climatic regions (Beck et al. 2018) in southwestern U.S. B = arid, C = temperate, D = cold, W = desert, S = steppe, h = hot, k = cold, s = dry summer, f = no dry season, a = hot summer; b = dry, warm summer.

frameworks. In most cases, a single regime was found from a few days to 0.5-1 h and, in some sites where sub-hourly measurements were available, an additional regime was detected from 0.5-1 h to a few minutes (e. g., Fraedrich and Larnder 1993; Deidda et al. 1999; Mandapaka et al. 2015; Verrier et al. 2011; Mascaro et al. 2013a). Seasonal differences in temporal scaling regimes have also been identified and attributed to different dominant weather systems (Molnar and Burlando 2008; Mascaro et al. 2014; Mascaro 2017). The evidence of P scaling has been also shown in space from 100-200 km to about 1 km and in space-time frameworks (Schertzer and Lovejoy 1987; Venugopal et al. 1999; Deidda 2000; Deidda et al. 2004; Mascaro et al. 2013b).

This body of knowledge has significantly advanced our understanding of short-duration P and allowed the development of sophisticated stochastic space-time P models. However, the datasets used in previous studies have been largely restricted to P observations collected during short-term field experiments or available at a few sites with limited spatial coverage and density. This is because rain gage P records at sub-daily resolution are still limited and sparse (Lewis et al. 2019; Morbidelli et al. 2020), while radar- and satellite-derived P estimates are heavily affected by several sources of errors, especially at high temporal resolutions (Michaelides et al. 2009; Krajewski et al. 2010). As a result, further analyses of high-quality, long-term P observations at high temporal and spatial resolutions are needed to confirm the validity of previous findings, examine aspects of short-duration P variability that have

received less attention, and support the operational use of space-time stochastic P models. These needs have become particularly important given recent evidence that short-duration P extremes have been intensifying due to global warming (Fowler et al. 2021; Prein et al. 2017b) and urbanization (Huang et al. 2022). Moreover, new knowledge on the statistics of short-duration P would be useful to validate convection-permitting atmospheric models that are being increasingly applied to study the mechanisms driving changes in short-duration P (Chen et al. 2021; Prein et al. 2017a).

Two important statistical properties of short-duration P that have received relatively less attention are the spatiotemporal correlation structure (STCS) and the distribution of the intermittent process of zero and nonzero P values. Previous work has focused on either the spatial correlation of P within short distances (~25 km) or the temporal (serial) correlation at single sites (Ciach and Krajewski 2006; Habib et al. 2001; Mascaro 2017; Zawadzki 1973; Marani 2005; Jameson 2021; Schleiss et al. 2011; among others). Changes in correlation structure of P for different combinations of space and time lags over large regions have not yet been explored. Recently, new flexible analytical models have been proposed by Papalexiou and Serinaldi (2020) and Papalexiou et al. (2021) to characterize the STCS of P, but these have not been tested yet against observations at fine temporal scales. Other recent studies have suggested single and two-component parametric distributions that could properly capture the body and tails of the distribution of short-duration

nonzero P (Papalexiou and Koutsoyiannis 2016; Emmanouil et al. 2021; Naveau et al. 2016). While promising, the recent methodological advancements on both the STCS and the marginal distribution of short-duration P require empirical corroboration and their value should be systematically investigated across different time scales, seasons, and sites.

These research needs are addressed in the study which has the main goal of advancing the ability to characterize and model the STCS and marginal distributions of short-duration P. To robustly investigate these statistical properties, we analyze long-term (>20 years), high-resolution (30-min) P records from a network of rain gages in central Arizona, which, to our knowledge, has one of the largest densities and spatial coverages in the world. This study region is compelling due to the strong seasonality of the P regime and the effect of orography which lead to marked variability in the statistical properties of P (Mascaro 2017, 2018, 2020).

We address the following research questions that have both scientific and practical implications and that provide arguably the first systematic characterization of STCS and marginal distribution of P across multiple temporal scales with an extensive and high-quality 30-min dataset. (1) How does the STCS of P at durations < 24 h vary seasonally? (2) Can the STCS be considered homogenous and isotropic? (Homogeneous means that the function is spatially stationary across the region, while isotropic means that the correlation is only affected by the distance between two sites and does not depend on the direction along which the distance is computed). (3) Is there a parametric distribution that adequately describes the body and tails of the nonzero P marginal distribution across multiple P durations? (4) Does the presence of serial correlation in shortduration P series significantly affect the estimation of the distribution parameters? And (5) how do the distribution parameters vary seasonally and spatially, and can they be regionalized? To answer these research questions, we perform a set of Monte Carlo experiments with the Complete Stochastic Modeling Solution (CoSMoS; Papalexiou 2018; Papalexiou and Serinaldi 2020; Papalexiou et al. 2021; Papalexiou 2022), which allows for the stochastic simulation of P time series at multiple sites that preserve prescribed marginal distributions and STCS. While these research questions are investigated in central Arizona, our methodological framework provides new insights into the space-time P variability at any location and provides key information to increase the reliability of space-time simulations of short-duration P.

2. Study Area and Dataset

Our study region is in central Arizona and includes the Phoenix Metropolitan area (Fig. 1a), where the Flood Control District of Maricopa County (FCDMC) has deployed a network of rain gages to monitor intense storms. The gages were progressively installed since 1980, eventually reaching the current number of 365. In this study, we use records of 223 gages with more than 20 years of observations (Fig. 1b). The gages cover a region of \sim 29,600 km² that mainly encompasses the Sonoran Desert at low elevations from 200 to 700 m above the sea level (ASL) and extends up to the southwestern portion of the Mogollon Rim at 2325 m ASL. Most gages are in urban areas (~2000 km²) with a density of 4.3 gauges per 100 km²; when considering the entire region, the density decreases to \sim 1 gauge per 100 km². The distribution of the inter-gage distance is presented in Fig. 1c, demonstrating that this network allows characterizing with unprecedented detail the spatial variability of P statistical properties, including correlation structure and marginal distribution.

The climate in this region of the desert southwestern U.S. is hot and arid. According to the Köppen-Geiger classification, the climate is categorized as BWh in most of the region, with smaller portions classified as BSh, BSk, and Dsb as the elevation increases (Fig. 1d; acronyms defined in its caption). The rainfall regime is strongly seasonal. Summers are dominated by the North American Monsoon (NAM) from July to September (Adams and Comrie 1997), during which short-lived (<1 h),

spatially localized thunderstorms occur with moderate-to-high rainfall intensities according to a diurnally modulated cycle. Winters, defined here from November to March, are characterized by westerly flow and extended dry periods that are occasionally interrupted by cold fronts that may cause large-scale storm systems controlled by dynamical lifting resulting in low-to-moderate rainfall intensities. These storms tend to be widespread and often cover the entire region and last for a few days. Previous studies (Mascaro 2017, 2018, 2020) have investigated several statistical properties of the rainfall regime in the region; their findings inform the new research directions pursued in this work.

3. Methods

3.1. Data processing

The FCDMC provides P data in a raw format containing the tipping instants in seconds, with a resolution of 1 mm for each tip. We obtain the rainfall time series at different temporal resolutions, $\Delta t = 0.5, 1, 2, 3, 6$, 12, and 24 h, using the method described by Mascaro et al. (2013), which limits the discretization of the signal caused by the commonly used box counting. Unfortunately, we find that the resolution of the gage bucket of 1 mm is quite coarse and limits the effectiveness of the smoothing procedure. Therefore, the P time series exhibit a considerable fraction of repeated values that are multiples of $1/\Delta t$ mm/h, which affect the comparison of the observed P statistics with those of the non-discretized synthetic samples generated with CoSMoS. We partially address this issue (see results) by rounding off the synthetic samples through a procedure based on Deidda (2007) that involves (1) estimating the percentage of observed measurements rounded off at multiples of $1/\Delta t$ mm/h, and (2) adopting these percentages to round off the corresponding synthetic samples. Given the different storm-generating mechanisms described in Section 2, analyses are conducted separately for summer (July-September) and winter (November-March).

3.2. Spatiotemporal correlation structure

The spatiotemporal correlation structure (STCS) describes the correlation (here, linear) between two random variables lagged by time τ (in hours) and placed at a distance δ (in km) (Papalexiou and Serinaldi, 2020). In symbols: $\rho_X(\tau,\delta) = \text{cor}[x(t,s_i),x(t+\tau,s_j)]$, with t being any time instant, and δ the Euclidian distance between locations s_i and s_j . Here, we model the STCS of P using a parametric form emerging from the Clayton Copula and the Weibull survival function (Papalexiou and Serinaldi, 2020). The Clayton-Weibull STCS is stationary and isotropic, and given by:

$$\rho_X(\tau, \delta; \theta) = \left\{ \exp\left[\theta \left(\frac{\delta}{b_S}\right)^{c_S}\right] + \exp\left[\theta \left(\frac{\tau}{b_T}\right)^{c_T}\right] - 1 \right\}^{-1/\theta}, \tag{1}$$

where $\theta = [b_S, c_S, b_T, c_T, \theta]$ is the parameter vector (note that the indices S and T stand for space and time, respectively). To estimate θ , we compute: (1) the empirical correlation matrixes of the gage records at different time lags, $[R^{(\Delta t,k)}]$, whose generic element $r_{ij}^{(\Delta t,k)}$ is the Pearson correlation coefficient between the P signal at resolution Δt at gage i and the P signal at the same resolution lagged by $\tau = (k \cdot \Delta t)$ at gage j (where k is the lag index ranging from 0 to the number of investigated lags, p); and (2) the distance matrix, [D], whose generic element, d_{ij} , is the Euclidian distance between gages i and j. We then use these matrixes to solve the least-square-regression equation:

$$\widehat{\boldsymbol{\theta}} = \operatorname{argmin}_{\boldsymbol{\theta}} f : \sum_{i=1}^{n-1} \sum_{j=i+1}^{n} \sum_{k=0}^{p} \left[r_{ij}^{(\Delta t,k)} - \rho_X (k \Delta t, d_{ij}; \boldsymbol{\theta}) \right]^2, \tag{2}$$

where the sum over i and j is used to include the terms in the upper triangle of the symmetric matrixes. The calculations are performed in MATLAB® using the function fit.

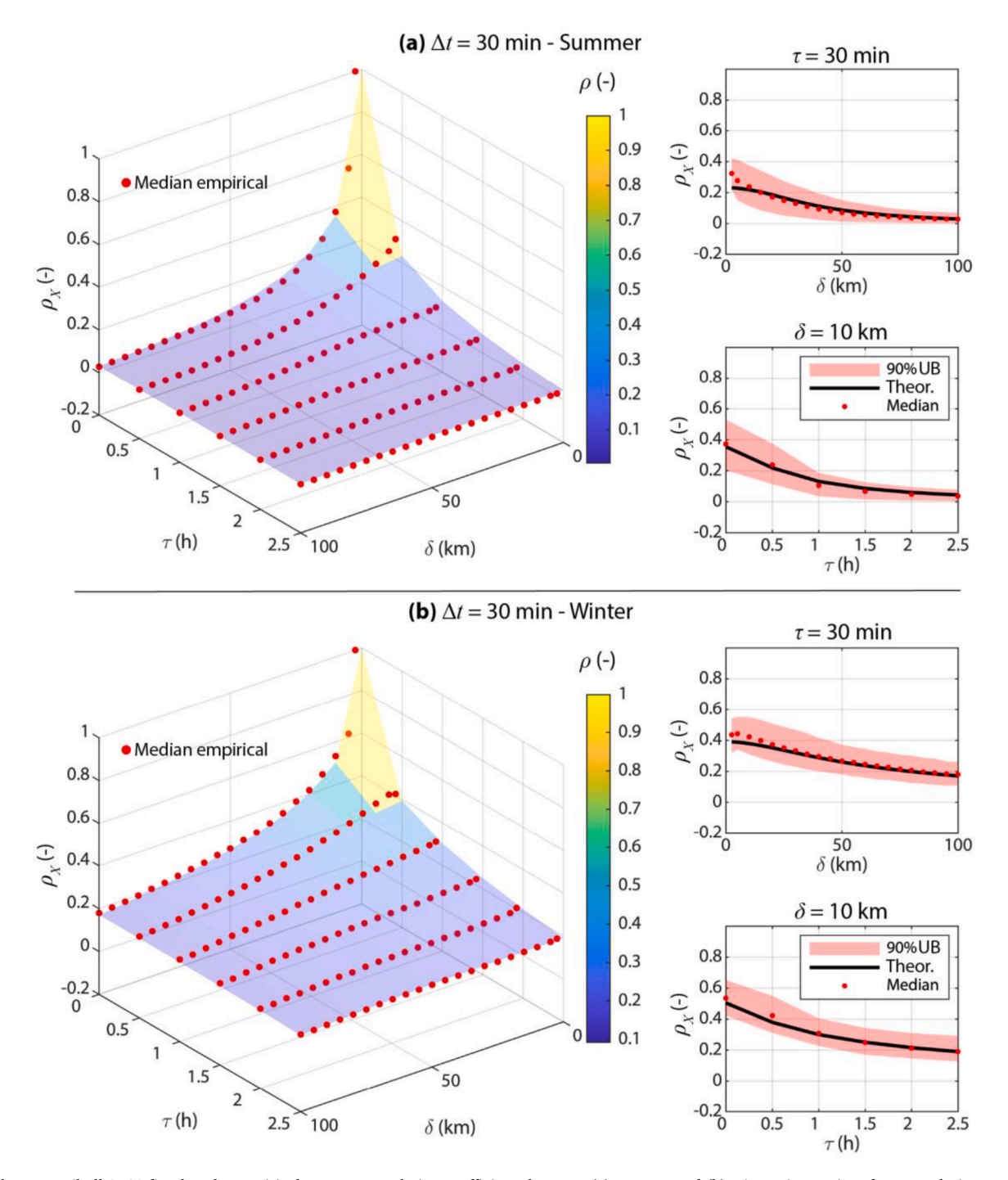


Fig. 2. Clayton-Weibull STCS fitted to the empirical Pearson correlation coefficients between (a) summer and (b) winter time series of P at resolution $\Delta t=30$ min observed at pairs of gages for different temporal lags, τ , and spatial distances, δ . Each panel displays (1) the theoretical surface with colors based on the value of ρ_X along with the median empirical correlation coefficients, and (2) two cross sections of the theoretical surface for fixed values of $\tau=30$ min and $\delta=10$ km, along with the median and 90% uncertainty band (UB) of the empirical correlation coefficients across the gages.

3.3. Candidate marginal distributions and parameter estimation

When considered at small aggregation times, P is an intermittent process that includes zero and nonzero values. Its distribution is then characterized by a probability mass concentrated at zero, p_0 , and a continuous part that characterizes nonzero values. In symbols, if X is the random P variable at a given resolution Δt , its cumulative distribution function (CDF), $F_I(x)$ (with the subscript I referring to the "intermittent" process) is given by:

$$X \sim F_I(x) = p_0 + (1 - p_0) \cdot F(x),$$
 (3)

with F(x) being the CDF of nonzero P (i.e., valid for x>0). In this study, we estimate p_0 as n_0/n , with n_0 being the number of time steps where P is zero and n is the total number of time steps. For F(x), we explore the suitability of three-parameter distributions that have been shown flexible to capture left and right tails, as well as the body of the empirical distribution of positive hydrologic variables (Papalexiou and Koutsoyiannis 2012; Papalexiou 2022). These include the Generalized Gamma (\mathcal{SS}), Burr Type XII (\mathcal{B}_r XII), and Generalized Exponential Type 4 (\mathcal{SS} 4) distributions. Their CDFs are:

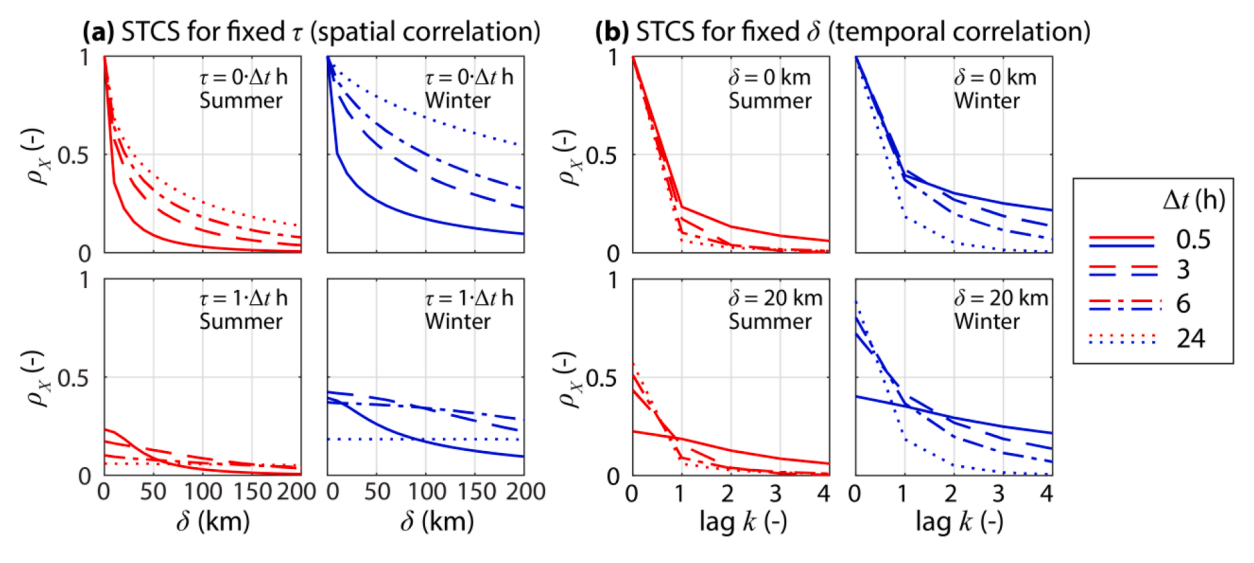


Fig. 3. Clayton-Weibull STCS of summer (red) and winter (blue) P for fixed values of (a) τ and (b) δ . In each panel, the STCSs are shown for four Δt 's using different line styles. To compare multiple Δt 's in panels (b), the lag k has been used in the x-axis instead of $\tau = k \cdot \Delta t$.

$$F_{\mathscr{T}\mathscr{T}}(x) = 1 - \Gamma\left(\frac{\gamma_1}{\gamma_2}, \left(\frac{x}{\beta}\right)^{\gamma_2}\right) / \Gamma\left(\frac{\gamma_1}{\gamma_2}\right),\tag{4}$$

$$F_{\mathscr{B}_{r}XII}(x) = 1 - \left[1 + \gamma_2 \left(\frac{x}{\beta}\right)^{\gamma_1}\right]^{-\frac{1}{\gamma_1 \gamma_2}},$$
 (5)

$$F_{\mathscr{ZZ}4}(x) = 1 - \left\{ \left[\exp\left(\left(\frac{x}{\beta}\right)^{\gamma_1}\right) - 1 \right]^{\gamma_2} + 1 \right\}^{\frac{1}{\gamma_2}}.$$
 (6)

These distributions are defined for $x \ge 0$; $\gamma_1 > 0$ and $\gamma_2 > 0$ are parameters controlling the shape of the distribution, and $\beta > 0$ is the scale parameter; $\Gamma(\cdot,\cdot)$ and $\Gamma(\cdot)$ denotes the incomplete gamma and gamma functions, respectively. Parameters are estimated using the numerical approach recently proposed by Zaghloul et al. (2020) based on the method of L-moments (Hosking and Wallis 1997). Details are provided in Appendix A. The suitability of the distributions is evaluated graphically with the L-moment ratio diagram and further assessed quantitatively via two goodness-of-fit (GOF) metrics reported in Appendix B.

3.4. Monte Carlo experiments with CoSMoS

We design Monte Carlo experiments based on the version of the Complete Stochastic Modeling Solution (CoSMoS) for multisite stochastic simulations of P time series that preserve prescribed space-time correlation structure and marginal distribution of P Papalexiou and Serinaldi 2020). This version of CoSMoS is briefly described in Appendix C. The experiments are used to investigate (1) the homogeneity and isotropy of the STCS in each season, and (2) the spatial variability of the distribution of the intermittent P process. For each Δt , an ensemble of synthetic time series is generated at the 223 gage locations with the same observed record lengths under prescribed STCS and marginal P distributions. The statistical properties of the synthetic time series are then compared to the observations. An additional Monte Carlo experiment is carried out to test the effect of serial correlation on parameter estimation for the distribution of nonzero P. This involves the generation of long-term times series at a single site with prescribed serial correlation (i.e., the STCS with $\delta = 0$) and marginal P distribution. Further details are provided in the next section.

4. Results

4.1. Spatiotemporal correlation structure: seasonal differences and effect of time aggregation

The Clayton-Weibull STCS is fitted to the empirical Pearson correlation coefficients for summer and winter P. As an example, results for $\Delta t = 0.5$ h are reported in Fig. 2. Visual inspection of the STCS surface and the cross sections for fixed values of τ and δ (chosen as examples) suggests that the Clayton-Weibull analytical model captures very well the median empirical correlation structure of P in the two seasons. This is true for all Δt 's (as an example, results for $\Delta t = 6$ h are shown in Fig. S1 in the Supplementary Material), with the root-mean-square error between empirical and theoretical STCSs ranging from 0.02 to 0.04 across all cases. The estimated parameters of the Clayton-Weibull STCS for all Δt 's are reported in Fig. S2. Given its effect on both the spatial and temporal correlation functions, we investigated the role of the θ parameter and found it to depend on the values of the other four parameters and to be, overall, relatively minor and more significant for the spatial correlation at $\tau \ge 1 \cdot \Delta t$; additional considerations are provided in Figs. S3 and S4.

Given its ability to represent the empirical STCS across all cases, we use the Clayton-Weibull model to explore seasonal differences of the P correlation structure as a function of Δt . To this end, we plot in Fig. 3 the Clayton-Weibull STCS for fixed values of τ and δ for $\Delta t = 0.5$ h, which is the characteristic timescale of single convective storms, and for $\Delta t = 3$, 6, and 24 h, which capture the behavior of larger single and multiple storms. We first note that, for any given Δt , ρ_X of all spatial (fixed τ) and temporal (fixed δ) correlation functions are higher in winter than in summer. This occurs because winter events are longer and more widespread, whereas summer monsoonal storms are more localized in time and space and intermittent (higher probability of zero P). The spatial correlation of P with no temporal lag ($\tau = 0 \cdot \Delta t$) shows that ρ_X increases with Δt in both seasons (Fig. 3a; top panels). This is expected since, as the P signal is aggregated over larger time steps, multiple storm "cells" may occur over a bigger spatial domain and there is a higher chance that nonzero P is simultaneously observed at sites located at large distances. If we instead consider the spatial correlation of temporally lagged ($\tau = 1$ \cdot Δt) P series (Fig. 3a; bottom panels), the role of Δt changes dramatically with similar impacts in the two seasons. For the largest $\Delta t = 24$ h, ρ_X drops to a very low value that is constant with δ , suggesting that in our study region storms rarely last for more than 24 h. For $\Delta t = 0.5$ h, ρ_X

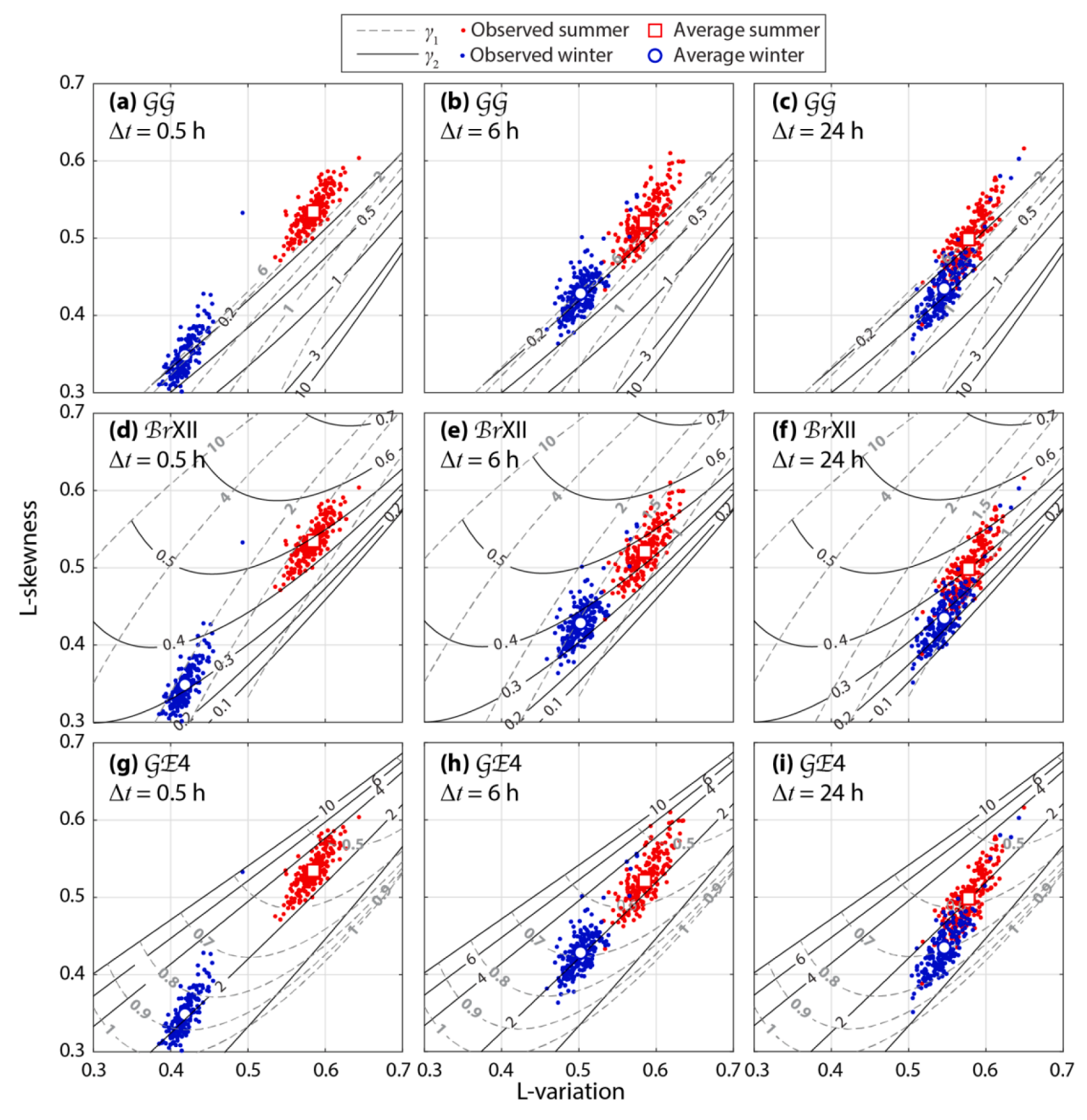


Fig. 4. L-moment ratio diagrams (i.e., the relation between L-variation and L-skewness) for observed P records at resolution $\Delta t = 0.5$ h, 6 h, and 24 h in summer and winter, along with the theoretical values of the (a)-(c) \mathcal{GG} , (d)-(f) \mathcal{B}_r XII, and (g)-(i) \mathcal{E}_r 4 distributions, plotted through contour lines for different combinations of the shape parameters γ_1 and γ_2 . The larger markers are the sample means of the L-moments.

declines but its values are nonnegligible for $\delta \leq 50$ km, especially in winter. The behavior of the spatial correlation for $\Delta t = 3$ h and 6 h is intermediate between the largest and smallest Δt 's discussed above.

As expected, the temporal correlation for $\delta=0$ km (i.e., the serial correlation functions; Fig. 3b, top panels) for a given dimensionless lag k increases in both seasons as Δt is reduced. In other words, as we consider shorter time steps, there is a higher chance that P observations at the same location are similar within a few time steps. The temporal correlation evaluated at sites at a distance $\delta=20$ km (Fig. 3b, bottom panels) is substantially similar to that for $\delta=0$ km, except for k=0 where ρ_X is significantly lower than 1 for all Δt 's, with a more significant drop observed for $\Delta t=30$ min because of the smaller spatial coverage of single storms.

In summary, the spatial correlation of P for $\tau = 0 \cdot \Delta t$ (Fig. 3a, upper panels) declines faster as the resolution increases (i.e., lower Δt),

whereas the opposite is true for the temporal correlation of P for $\delta=0$ (Fig. 3b upper panels). This behavior is reversed for lagged spatial correlations (Fig. 3a, lower panels) and fixed-distance lagged correlations (Fig. 3b, lower panels).

4.2. Marginal distribution of short-duration precipitation

4.2.1. Selection of parametric distribution of nonzero precipitation

We first focus on the distribution of nonzero P, F(x), and evaluate the suitability of the \mathcal{GG} , \mathcal{B}_rXII , and $\mathcal{GE}4$ theoretical models. Fig. 4 presents the L-moment ratio diagrams (L-skewness vs. L-variation) for three representative Δt 's; each panel displays the sample L-moments along with surfaces obtained for different combinations of the shape parameters γ_1 and γ_2 for each of the three considered distributions (note that distributions with a single shape parameter would instead be

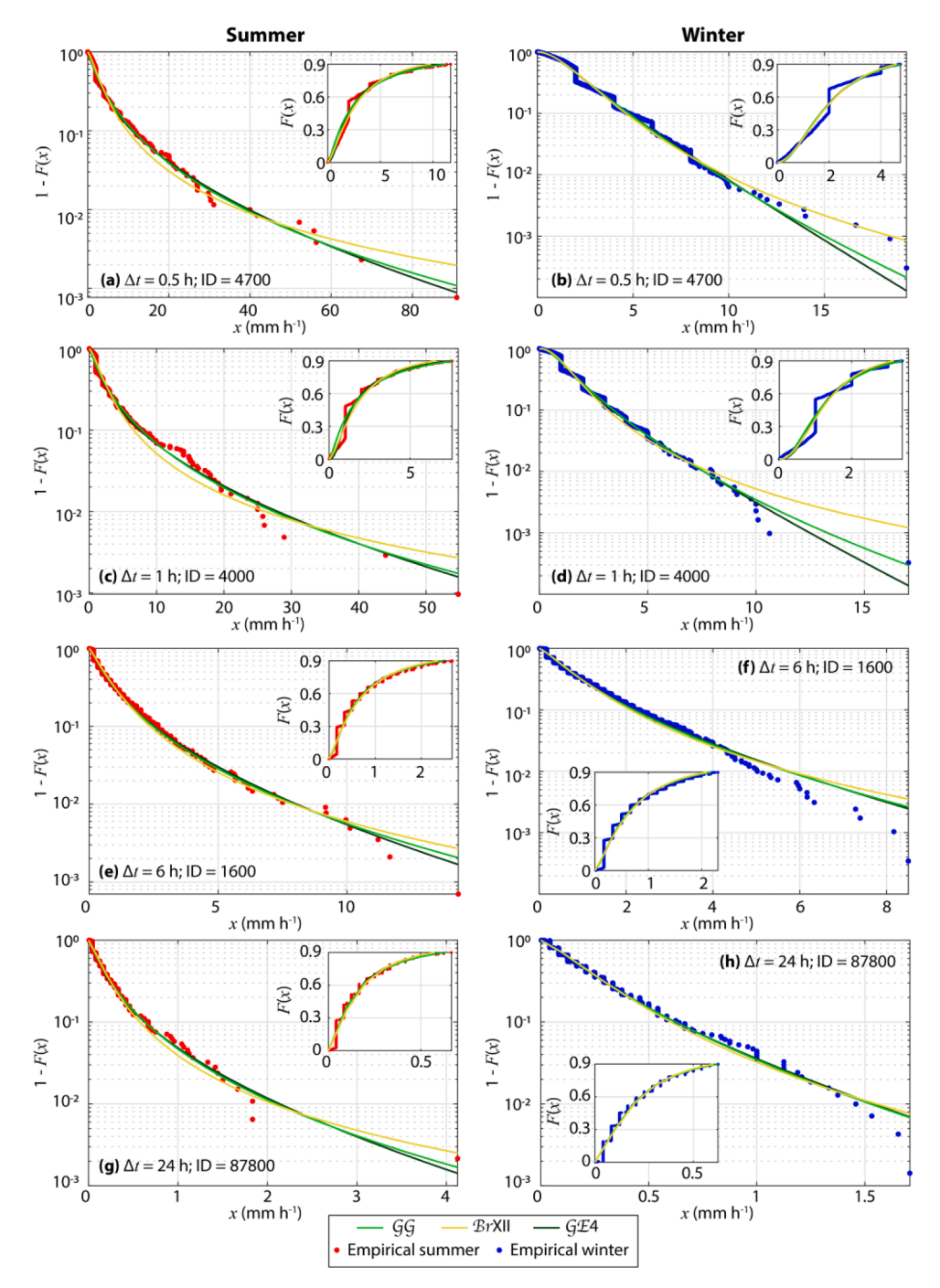


Fig. 5. Empirical and fitted theoretical ($\mathscr{G}\mathscr{F}$, \mathscr{B}_rXII , and $\mathscr{E}\mathscr{E}$ 4) CDFs of nonzero P observed at gages with ID (a)-(b) 4700 ($\Delta t = 0.5$ h), (c)-(d) 4000 ($\Delta t = 1$ h), (e)-(f) 1600 ($\Delta t = 6$ h), and (g)-(h) 87800 ($\Delta t = 24$ h) for (left) summer and (right) winter. The CDF is shown as survival function in the semi-logarithmic plane to highlight the fitting on the right tail. The zoom on the body of the CDF ($F(x) \le 0.9$) is shown in the insets. The empirical CDF is plotted with the Hazen plotting position.

represented by a curve in the L-skewness/L-variation space). The L-moments of P records exhibit seasonal differences, with winter P characterized by lower values of both L-ratios than summer P. The differences are marked at lower Δt and tend to be smaller as Δt increases. The \mathscr{GF} is the least flexible distribution and its surface does not fully include the sampling variability of the L-ratios. On the other hand, the $\mathscr{B}\textsc{rXII}$ is the most flexible. However, its shape parameters for low Δt in summer $(\gamma_2>0.5)$ lead to distributions with infinite variance, which is an undesirable condition for modeling time series stochastically since unrealistically large events could be frequently generated. The $\mathscr{GE}4$ has intermediate flexibility and captures all possible combinations of the sample L-moments while having always finite moments.

The GOF of the distributions is further evaluated by plotting in Fig. 5 the empirical CDFs of nonzero P at different Δt 's in the two seasons at four representative gages along with the fitted theoretical distributions. We first note that, despite the presence of several repeated values that are multiples of $1/\Delta t$ mm/h, the fitting of the distributions through the method of L-moments is quite effective. All parametric models capture very well the body of the empirical CDF ($F(x) \leq 0.9$; shown in insets). Differences emerge in some cases at the right tail, with \mathscr{B}_r XII exhibiting heavier tails and the largest deviations from the empirical distribution. This is quantified by the values of the GOF metrics of Appendix B, W^2 and RelMSE, reported in Table 1 for the examples of Fig. 5. Boxplots summarizing the GOF metric across all gages are displayed in Fig. S7,

Table 1
GOF metrics for the cases shown in Fig. 5.

Gage ID (Δt)	Season	GOF Metric	$\mathcal{G}\mathcal{G}$	BrXII	G E 4
4700	Summer	W^2	1.81	1.21	0.95
(0.5 h)		RelMSE	$0.97 \ 10^{-2}$	$2.04 \ 10^{-2}$	$0.73 \ 10^{-2}$
	Winter	W^2	4.50	4.11	4.19
		RelMSE	$1.84 \ 10^{-2}$	$2.19 \ 10^{-2}$	$1.79 \ 10^{-2}$
4000	Summer	W^2	2.70	2.11	1.73
(1 h)		RelMSE	$1.58 \ 10^{-2}$	$3.21 \ 10^{-2}$	$1.44 \ 10^{-2}$
	Winter	W^2	7.12	6.61	6.33
		RelMSE	$1.83 \ 10^{-2}$	$3.89 \ 10^{-2}$	$1.72 \ 10^{-2}$
1600	Summer	W^2	1.41	1.63	1.46
(6 h)		RelMSE	$1.12\ 10^{-2}$	$2.21 \ 10^{-2}$	$0.93 \ 10^{-2}$
	Winter	W^2	3.02	3.39	3.20
		RelMSE	$4.56\ 10^{-2}$	$8.27 \ 10^{-2}$	$4.17 \ 10^{-2}$
87800	Summer	W^2	0.46	0.51	0.46
(24 h)		RelMSE	$1.09 \ 10^{-2}$	$1.48 \ 10^{-2}$	$1.34 \ 10^{-2}$
	Winter	W^2	0.38	0.44	0.41
		RelMSE	$4.73 \ 10^{-2}$	$6.41 \ 10^{-2}$	$4.97 \ 10^{-2}$

which further indicate that the discrepancies of the \mathscr{B}_rXII in the right tail, measured by RelMSE, are higher for lower Δt . Interestingly, even if the region of theoretical L-moments for the \mathscr{GS} does not capture the sample points for $\Delta t=0.5$ h (see Fig. 4a), the closest pairs of γ_1 and γ_2 to the corresponding sample point returned by the parameter estimation method leads to a fairly good fit to the observed CDF. Given the overall higher performance, in the following analyses, the $\mathscr{GE}4$ is used as the marginal distribution for nonzero P.

4.2.2. Effect of serial correlation on parameter estimation

For low Δt , the serial correlation of the P time series can be high, and the assumption of independent events may not hold. From the practical standpoint, this implies that the effective sample size is reduced, thus increasing uncertainty when estimating the marginal distribution parameters. To evaluate this, we perform Monte Carlo experiments where CoSMoS is used to generate two ensembles of $N_{ens}=100$ long-term

serially correlated and uncorrelated time series, respectively, of intermittent P at $\Delta t=0.5$ h. The highest resolution is chosen since it has the strongest serial correlation (see Fig. 3b). For these ensembles, we use (1) the mean p_0 across the gages; (2) the $\mathscr{SE}4$ distribution for F(x) with mean values of γ_1 , γ_2 , and β ; and (3) the serial correlation provided by the Clayton-Weibull STCS, $\rho_X(\tau, \delta=0)$. This is done separately for summer and winter, generating in each case 200 consecutive seasons (i. e., a dataset of 200 years of observations). Fig. 6a shows the theoretical serial correlations and marginal distributions of the intermittent P process, $F_I(x)$, used to apply CoSMoS in the two seasons, along with the corresponding empirical functions from one of the synthetic time series. The correspondence is remarkable, indicating that the CoSMoS framework reproduces very well these statistical properties of the P signal.

Parameters γ_1 , γ_2 , and β are then re-estimated by fitting the $\mathcal{SE}4$ to the nonzero P of each synthetic time series for the number of seasons, m, ranging from 10 to 200. Results are presented in Fig. 6b, which shows

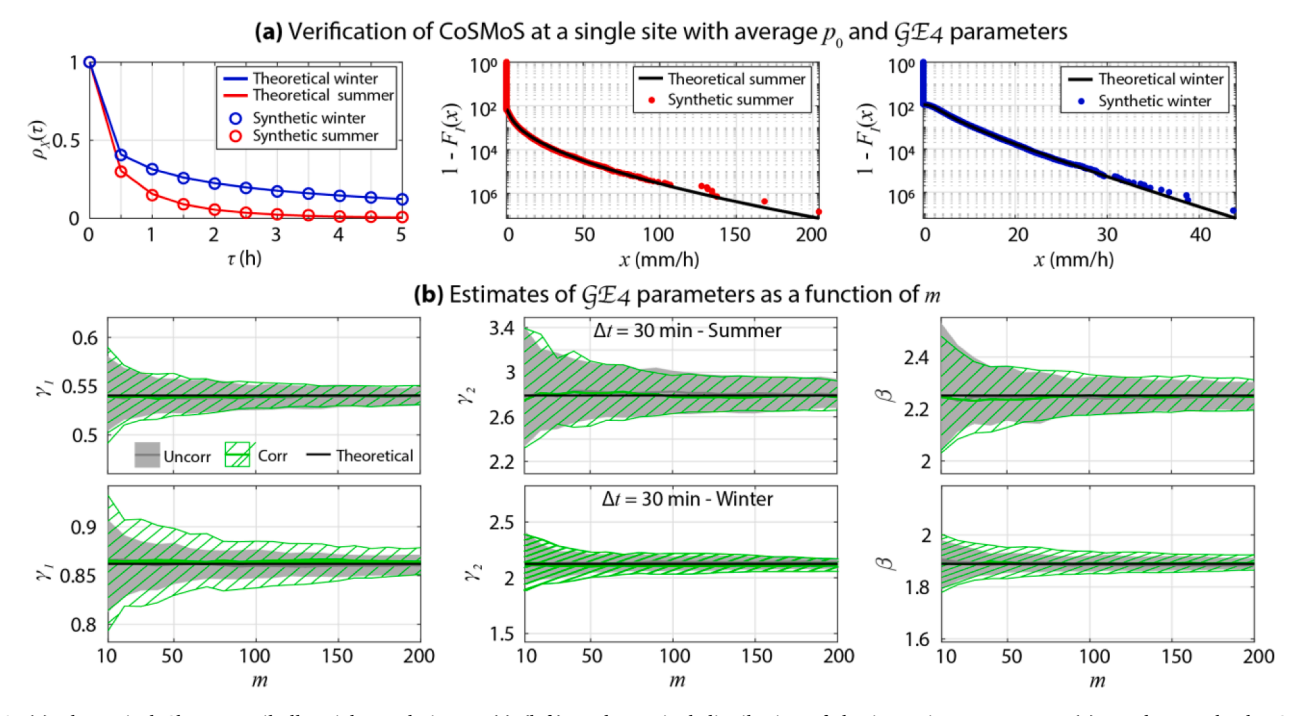


Fig. 6. (a) Theoretical Clayton-Weibull serial correlation, $ρ_X(τ)$ (left), and marginal distribution of the intermittent process, $F_f(x)$, used to apply the CoSMoS framework for generating time series in summer (middle) and winter (right), along with empirical values computed from a synthetic time series. (b) Comparison of median and 90% confidence intervals of \mathscr{E} 4 parameters estimated from 100 synthetic serially correlated (Corr) and uncorrelated (Uncorr) time series generated with CoSMoS for $\Delta t = 30$ min in summer (top panels) and winter (bottom panels) for the number of seasons, m, ranging from 10 to 200. See main text for details.

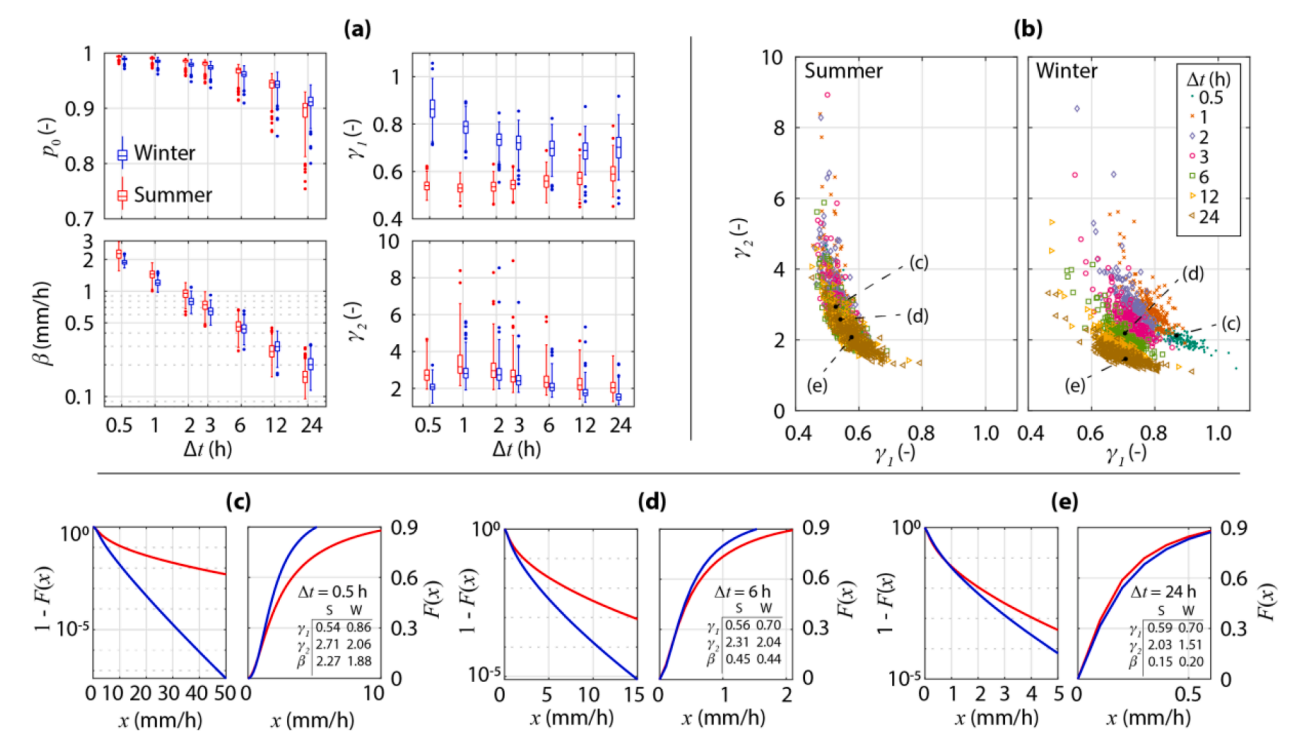


Fig. 7. (a) Boxplots summarizing the empirical distribution of p_0 and the $\mathscr{SE}4$ parameters, γ_1 , γ_2 and β , fitted to winter (blue) and summer (red) nonzero P observed at the 223 gages as a function of the resolution, Δt . (b) Scatterplot between γ_1 and γ_2 for all Δt 's in summer (left) and winter (right). (c)-(e) $\mathscr{E}4$ distribution for the median parameter values (reported in insets and shown in panel b with arrows) for $\Delta t = 0.5$, 6, and 24 h, respectively, represented as exceedance (left) and nonexceedance (right) probabilities.

the 90% confidence intervals of the estimated parameters. In all cases and for all m's, the estimates are unbiased, and the uncertainty of correlated and uncorrelated series is the same, even for low m. The only exception is the case of γ_1 in winter, where the uncertainty of the correlated series is slightly larger likely because of the stronger serial correlation. Overall, these experiments suggest that the considered samples are long enough that the presence of serial correlation does not significantly affect parameter estimation. Therefore, there is no practical need to apply techniques to identify statistically independent events, as in principle required by the assumption of independent and identically distributed (i.i.d.) variables. This result was verified for all Δt 's (not shown). If, in future applications, this turns out not be the case due to stronger serial correlations, smaller samples, or the use of a different probability distribution, the proposed Monte Carlo framework could be used to identify strategies to extract an independent sample from the original time series or bias correct the parameter estimates.

4.2.3. Seasonal variability of the marginal distribution as a function of time aggregation

Fig. 7a presents the boxplots of p_0 and the $\mathscr{SE}4$ parameter estimates at the 223 gages for all Δt 's. Seasonal differences emerge for all parameters. The probability of zero P, p_0 , is slightly higher in summer than winter when the signal is aggregated up to $\Delta t = 6$ h; the opposite is true for longer-time aggregations. Moreover, the relation between p_0 and Δt is linear ($R^2 > 0.95$; not detectable in the semilogarithmic plot of Fig. 7a) with a mean slope of -4.3×10^{-3} (-3.3×10^{-3}) h⁻¹ in summer (winter). The scale parameter β is (1) relatively larger for summer P at smaller Δt 's, (2) similar in the two seasons at intermediate $\Delta t = 6$ h, and (3) higher for winter P at larger aggregation times. In addition, β exhibits a scaling relationship with Δt (highlighted through the log-log plot) with a slope of -0.68 (-0.57) in summer (winter). Focusing on the shape parameters, γ_1 is larger for winter than summer P, while the opposite is true for γ_2 but with less notable differences. As expected by the location of the L-moments estimates (see Fig. 4), neither parameter exhibits

significant variations with Δt when considering summer P, except for slightly higher values of γ_2 for $\Delta t=1$ h. Larger variations of the shape parameters with Δt are instead observed for winter P, particularly for γ_1 that decreases between $\Delta t=0.5$ h to $\Delta t=6$ h.

We further investigate the relationship between the shape parameters as a function of the time aggregation in each season by plotting in Fig. 7b the scatterplots between γ_1 and γ_2 for all Δt 's. The two $\mathscr{GE}4$ parameters are inversely related in a nonlinear fashion. In summer, a single relation encapsulates the estimates for all Δt 's, with slightly higher (lower) values of γ_1 (γ_2) found for $\Delta t \ge 6$ h. In contrast, distinct relationships between the two parameters emerge in winter for each Δt . To visualize how these outcomes affect the shape of F(x), Fig. 7c-e display the $\mathscr{GE}4$ CDFs with the median parameter values for $\Delta t = 0.5, 6$, and 24 h in the two seasons, which are also depicted with arrows in Fig. 7b. The distribution of summer P is always heavy tailed, with very limited changes of its shape across Δt 's. Winter P is instead characterized by a distribution with much lighter tails than summer and whose heaviness gradually increases with Δt . Our sensitivity tests and the visual inspection of Fig. 7b indicate that (1) γ_1 exerts the largest control on the right tail, and (2) differences in β mainly affect the body of the distribution ($F(x) \le 0.9$).

4.2.4. Spatial variability of the marginal distribution

As a next step, we investigate whether the inter-gage variability of p_0 and \mathcal{S} &4 parameters results from sampling variability or is related to local physical factors. We find that p_0 has a rather constant value for elevation, z, lower than 400 m ASL and decreases linearly with z with a slope that is larger in absolute value (i.e., stronger orographic control) as Δt increases. This is shown in Fig. 8a-b for three Δt 's, while maps are reported in Fig. S8. The Pearson correlation coefficient (CC) with z is >0.81 across seasons and Δt 's. The scale parameter β is moderately related to z in a nonlinear fashion, as presented in the examples of Fig. 8c-d for three Δt 's and quantified by Spearman CC between 0.21 and 0.51 across all cases. For the shape parameters γ_1 and γ_2 , no significant

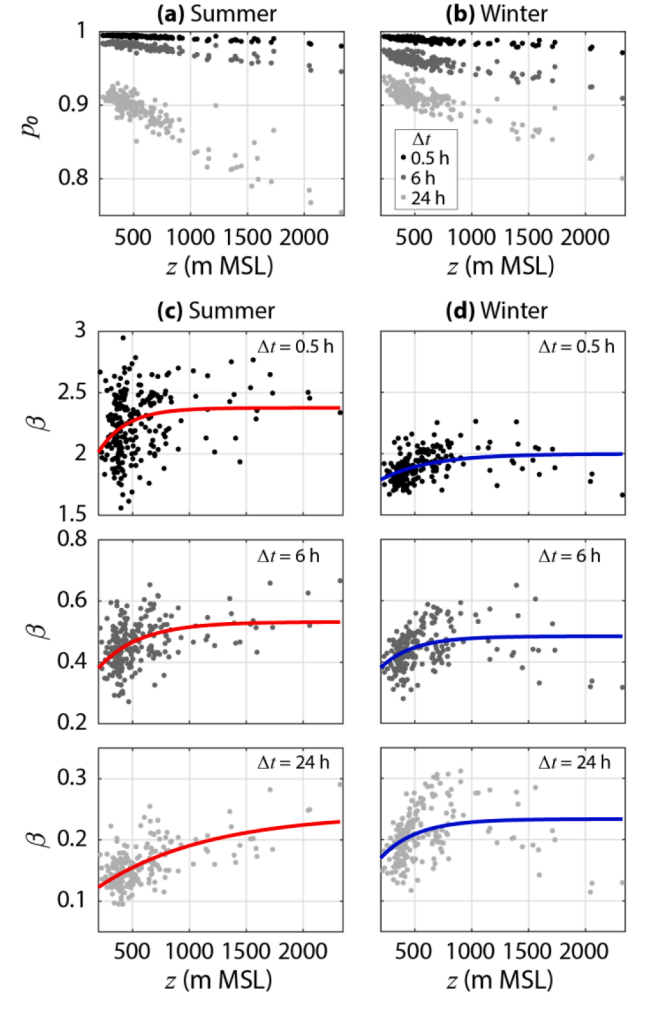


Fig. 8. (a)-(b) Relation between p_0 and gage elevation, z, in summer and winter, respectively, for $\Delta t=0.5$, 6, and 24 h. (c)-(d) Same as (a)-(b) but for β with the lines being the fitted nonlinear Eq. (9d).

relations are found with z or gage coordinates. Examples of maps of the three $\mathcal{GE}4$ parameters are reported in Figs. S5-S6.

4.3. Insights into the correlation structure and physical controls on short-duration precipitation through stochastic simulations with CoSMoS

The insights gained in the previous sections allow designing Monte

Carlo experiments with CoSMoS to investigate the following two hypotheses: (1) the STCS of short-duration P in the region could be considered spatially homogeneous and isotropic in each season; and (2) the spatial variability of the parameters of the marginal distribution, $F_I(x)$, is explained by a few regional relations. The latter ones are identified based on the empirical evidence presented in Section 4.2.4, which suggests that, for a given Δt and season, the shape of the nonzero P distribution, controlled γ_1 and γ_2 , can be considered constant, while the scale parameter β and p_0 are related to the elevation. This translates into the following relations for each Δt :

$$p_{0} = \begin{cases} p_{0,max} & z \leq z^{*} \\ p_{0,max} + m \cdot (z - z^{*}) & z > z^{*} \end{cases},$$
 (9a)

$$\gamma_1 = \bar{\gamma}_1$$
 (9b)

$$\gamma_2 = \bar{\gamma}_2 \tag{9c}$$

$$\beta = \beta_{m} - (\beta_{m} - \beta_{0}) \cdot e^{-q \cdot z} \tag{9d}$$

where $p_{0,max}$ and m are intercept and slopes of the linear relation, respectively, and $z^*=400$ m ASL; $\bar{\gamma}_1$ and $\bar{\gamma}_2$ are the $\mathscr{GE}4$ shape parameters corresponding to the sample mean L-variation and L-skewness across all gages (see Fig. 4g-i); and β_{∞} , β_0 , and q are coefficients of a decreasing exponential relationship linking the $\mathscr{GE}4$ scale parameter with z (see Fig. 8c-d). The latter one is the same analytical relation that was found by Mascaro (2018) to well capture the relation between z and the scale parameter of the generalized Pareto distribution used as a theoretical model of daily extreme P in this region. The values of the estimated coefficients and parameters of equations (9) in each season and Δt are reported in Table 2.

To evaluate these hypotheses, for each Δt , we perform two sets of simulations with CoSMoS, each consisting of the generation of 100 spatially and temporally correlated synthetic time series at the 223 gages with the same duration of the observed records. In the first set, parameters of $F_I(x)$ are specified using the at-site estimates (labeled Atsite), while, in the second set, parameters are obtained through the regional equations (9a-d) (labeled Regional). In both cases, the Clayton-Weibull model of Eq. (1) with parameters reported in Fig. S2 is used to estimate the STCS. The At-site simulations are expected to provide the best possible performance of this version of CoSMoS with a homogeneous and isotropic STCS. Our first hypothesis is then addressed by quantifying the discrepancies between the observed inter-gage correlations and those computed from the At-site synthetic time series. The second hypothesis is assessed by measuring the degree to which the performance of Regional in simulating the observed L-moments and empirical marginal P distributions degrades compared to At-site.

Fig. 9 shows, for three Δt 's and both seasons, the correlation coefficients between the observed P signals at all gage pairs for two

Table 2Values of estimated coefficients and parameters of equations (9).

		Δt (h)								
		0.5	1	2	3	6	12	24		
$p_{0,max}$	S	0.995	0.992	0.988	0.983	0.972	0.950	0.907		
	W	0.991	0.987	0.982	0.977	0.966	0.949	0.919		
m	S	-0.005	-0.010	-0.016	-0.018	-0.030	-0.047	-0.079		
(1/km)	W	-0.008	-0.013	-0.015	-0.018	-0.025	-0.039	-0.048		
$\bar{\gamma}_1$	S	0.54	0.53	0.53	0.54	0.55	0.57	0.58		
	W	0.86	0.78	0.73	0.71	0.69	0.68	0.69		
$\bar{\gamma}_2$	S	2.73	3.25	3.00	2.69	2.35	2.20	2.03		
	W	2.08	2.83	2.78	2.46	2.08	1.79	1.54		
β_{∞}	S	2.32	1.48	0.96	0.76	0.49	0.31	0.19		
	W	1.98	1.27	0.87	0.72	0.50	0.34	0.25		
β_0	S	1.61	1.03	0.66	0.54	0.34	0.20	0.12		
	W	1.59	1.00	0.66	0.51	0.33	0.22	0.14		
q	S	5.04	5.72	4.97	4.91	3.56	2.21	1.47		
	W	3.05	3.03	2.35	2.21	2.09	2.17	1.74		

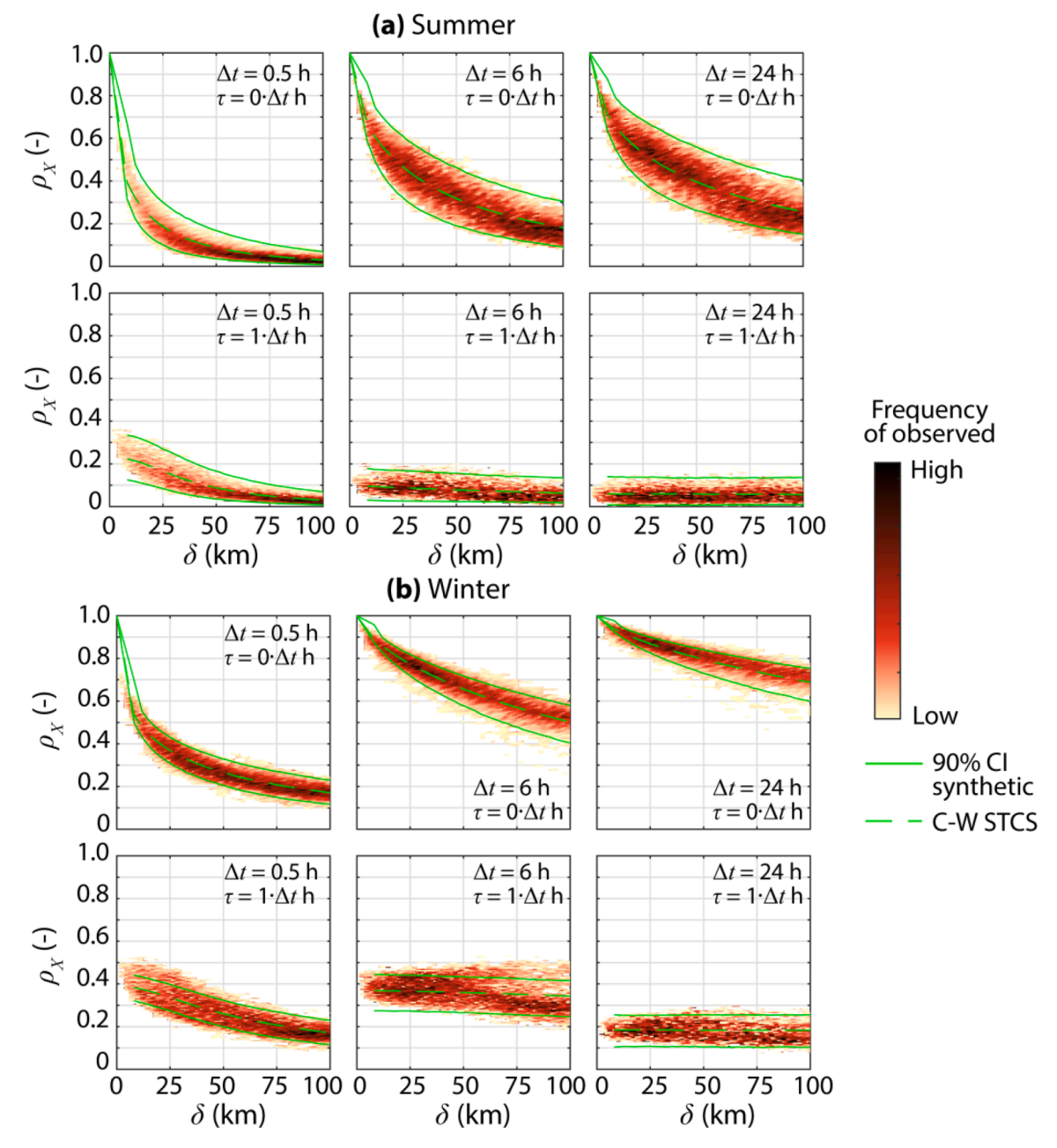


Fig. 9. (a) Pearson correlation coefficients between the observed summer P time series at temporal lags $\tau = 0 \cdot \Delta t$ (top) and $1 \cdot \Delta t$ (bottom), for $\Delta t = 0.5$ h (left), 6 h (middle), and 24 h (right) plotted as a function of inter-gage distance, δ , along with the 90% confidence interval (CI) derived from 100 At-site synthetic simulations with CoSMoS. (b) Same as (a), but for winter P. Given the large number of gage pairs, the observed values are plotted with colors based on the frequency of points.

temporal lags, τ , as a function of the inter-gage distance, δ , along with the 90% confidence interval (CI) derived from the 100 At-site simulations with CoSMoS (note that results are the same for Regional since the same analytical STCS is used in both experiments). In summer, a single analytical model for the STCS captures remarkably well the empirical values for all δ , τ , and Δt . Performances slightly degrade in winter (i.e., more cases have >10% of the observed correlations outside the CIs), especially for $\Delta t \geq 3$ h, but they are still satisfactory in most cases. These findings suggest that, in summer, the STCS of subdaily and daily P could be considered with high confidence homogeneous and isotropic, while a certain degree of nonhomogeneity and/or anisotropy exists in winter.

To investigate the second hypothesis, we first compare the L-moments ratio diagrams of the observed samples (same as Fig. 4) and one ensemble member of the Regional experiment. As shown in Fig. 10, the L-moments of the synthetic P signals exhibit a slightly larger spread than

the observed estimates and similar averages, indicating that the observed variability of these two statistics is within the sampling variability of the $\mathscr{C}4$ distribution with a single set of regional shape parameters. The larger spread of the synthetic L-moments might result from the observed P records having slightly smaller L-kurtosis than the synthetic ones (note that the L-kurtosis is not used in the estimation of the $\mathscr{C}4$ parameters); however, this issue should be further investigated through, e.g., ad-hoc Monte Carlo simulations. We then compare the observed CDFs of nonzero P with the 90% CIs of the synthetic samples. Results for the same gages of Fig. 5, chosen as examples, are displayed in Fig. 11 which shows that (1) the 90% CIs of At-site (gray lines) capture very well the observed CDFs across Δt 's and seasons, confirming the suitability of the $\mathscr{E}4$ distribution; and (2) the Regional simulations (black lines) exhibit somewhat degraded performance that is worse in some cases in winter (e.g., Fig. 11b,d,f). Moreover, there are a

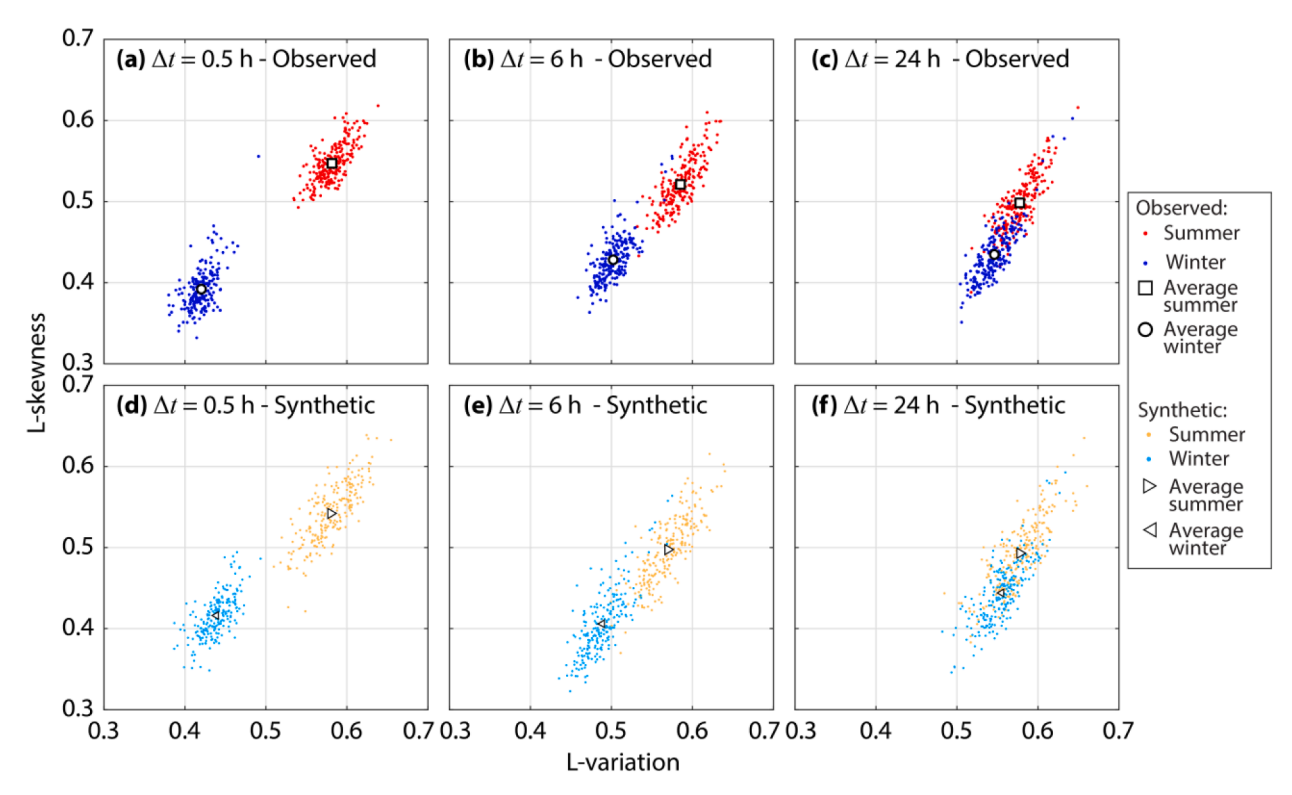


Fig. 10. L-moment ratio diagrams for (a)-(c) the observed records of P at resolution $\Delta t = 0.5$ h, 6 h, and 24 h in summer and winter, and (d)-(f) a synthetic simulation of the Regional experiment.

few cases where the visual assessment suggests that the simulation performance is good but the percent of observations outside the 90% CIs (labeled as '% out') is >10%. This occurs because the discretized measurements at low P values affect the shape of the CDF in a way that leads to several observed values being very close to but outside the 90% CIs of the simulations (see insets in Fig. 11), even after the latter ones have been rounded off at multiples of $1/\Delta t$ mm/h as described in the Methods.

These outcomes are confirmed and summarized in Fig. 12, where the mean across all gages of '% out' is reported for the entire CDF and for F(x) > 0.5 to eliminate the effect of the discretized measurements on this performance metric. The At-site simulations capture very well the observed CDFs in summer, as shown by the mean of '% out' always being $\leq 10\%$; for certain Δt 's in winter, the averaged '% out' is > 10% for the entire CDF but is dramatically reduced well below the 10% threshold for F(x) > 0.5. As expected, the performance of Regional lowers compared to At-site but is still accurate for F(x) > 0.5, except for $\Delta t \geq 3$ h in winter. Importantly, the extreme rain rates (F(x) > 0.95) are practically always included within the 90% CIs (not shown). Overall, these findings suggest that the elevation-dependent regional model of equations (9) allows capturing the variability of short-duration P across all Δt 's in summer and for most Δt 's in winter. Results also indicate that additional factors might be needed to fully explain the variability of winter P for $\Delta t \geq 3$ h.

5. Discussion

5.1. Summary of results in central Arizona

Our characterization of STCSs and marginal distributions reveal that important differences exist in the study region between the statistical properties of short-duration P in the two seasons. The distinct physical mechanisms driving summer and winter P lead to significant differences for the smallest $\Delta t = 0.5$ h, which progressively decrease as P is aggregated over larger Δt 's. Summer P is dominated by convective monsoonal thunderstorms, whose typical time scale is close to $\Delta t = 0.5$ h. These

storms are isolated in space and time, as revealed by the sharp drop of the spatial correlation at $\Delta t = 0.5$ h for $\delta < 50$ km (Fig. 3a, top) and the lag-1 serial correlation for $\Delta t > 0.5$ h (Fig. 3b, top). Summer P sampled at $\Delta t = 0.5$ h is characterized by high rain rates with intense extremes, as shown by the high scale parameter β and the heavy tail of the distribution (low γ_1 ; Fig. 7). The aggregation of short-lived thunderstorms at larger Δt 's impacts the statistical properties of the P signal in three different ways. First, it leads to increasingly higher spatial correlation because there are more chances that nonzero P is simultaneously observed at separate locations resulting from storm "cells" occurring at different times (Fig. 3a, top). Second, it causes a further drop in the serial correlation suggesting that multiple cells occur only within 1-2 h (Fig. 3b, top). Third, it leads to distributions that have gradually lower magnitudes of the more frequent events compared to winter P at the same Δt , but still intense extremes (heavy tail) which are likely controlled by a single storm with very high intensity occurring within Δt . This is shown by the fact that β decays faster with Δt for summer than winter (Fig. 7a), while γ_1 does not change significantly (Fig. 7b).

Winter P is dominated by frontal systems that occupy larger areas and last longer than monsoonal thunderstorms. This is quantified by (1) the spatial correlation being non-negligible at $\delta=200$ km even for the smallest Δt Fig. 3a, top), and (2) the lag-1 serial correlation being similar for $\Delta t \leq 6$ h Fig. 3b, top). Frontal systems lead to relatively low rain rates with little variance when P is sampled at $\Delta t \leq \sim 2$ h, as shown by smaller β than summer and the light tail of the distributions (i.e., high γ_1 ; Fig. 7). As P is accumulated over larger Δt 's, the magnitude of both more and less frequent events increases, as quantified by (1) β decaying slower with Δt compared to summer and becoming comparatively higher for $\Delta t > 6$ h, and (2) the tail of the distributions becoming heavier (i.e., γ_1 slightly decreasing).

The Monte Carlo simulations with CoSMoS under prescribed STCS and parameterizations of the marginal distribution provide further insights into the spatial variability of short-duration P. The hypothesis that the STCS of summer P is homogeneous and isotropic (Fig. 9a) cannot be rejected, likely because monsoonal thunderstorms are localized and

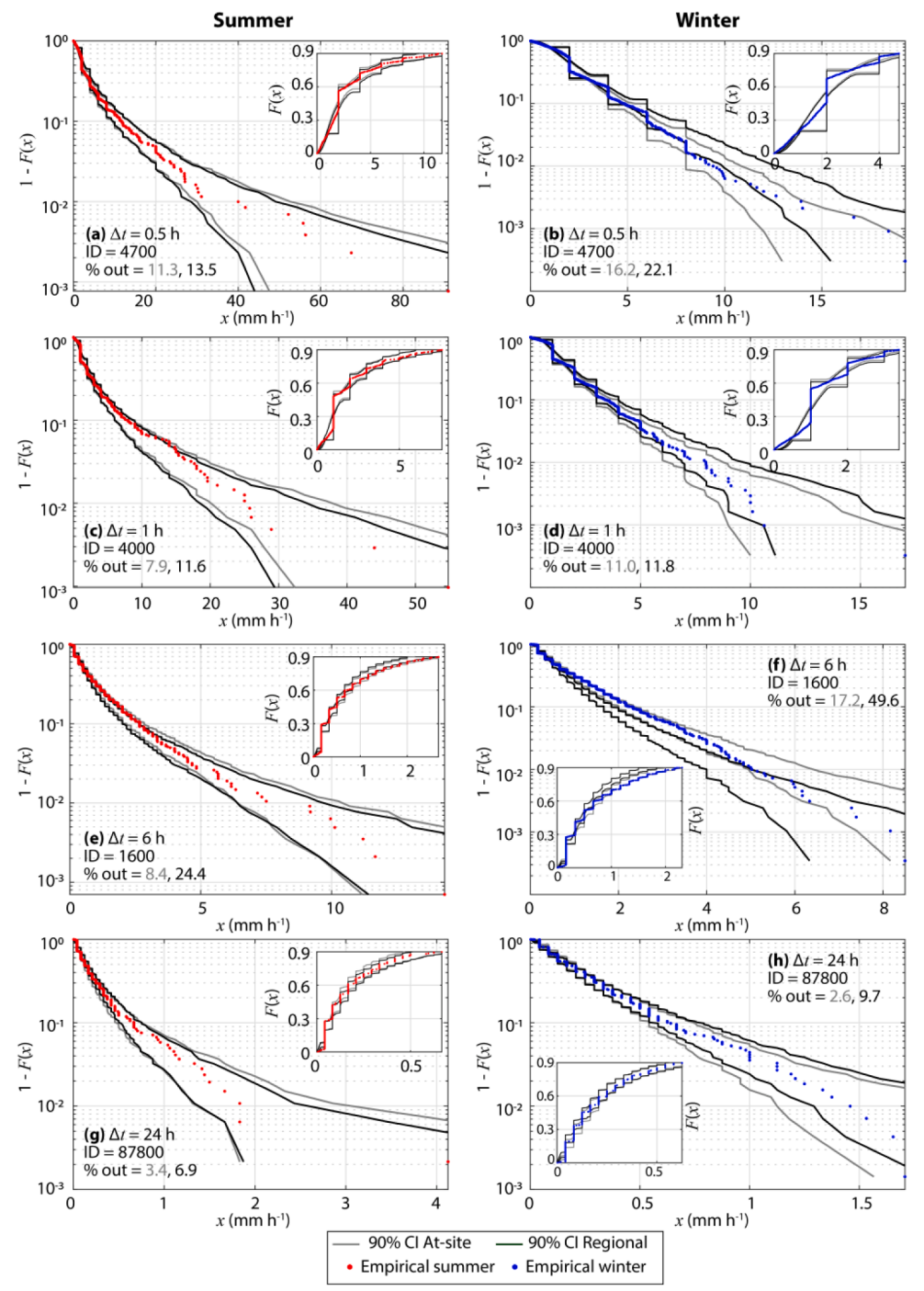


Fig. 11. Empirical CDFs of nonzero P observed at gages with ID (a)-(b) 4700 ($\Delta t = 0.5 \text{ h}$), (c)-(d) 4000 ($\Delta t = 1 \text{ h}$), (e)-(f) 1600 ($\Delta t = 6 \text{ h}$), and (g)-(h) 87800 ($\Delta t = 24 \text{ h}$) for (left) summer and (right) winter, along with 90% CI computed from At-site and Regional simulations (see main text for details). The zoom on the body of the CDF ($F(x) \le 0.9$) is shown in the insets. The percent of observed values outside the 90% CI ("% out") is reported in each panel with gray (black) text for At-site (Regional) simulations.

rather stationary, and do not exhibit dominant directions. The shape of the marginal distribution of P (controlled by γ_1 and γ_2) could be considered constant across the region (Fig. 10), similar to the growth curve used in regional frequency analysis of extreme P (Hosking and Wallis 1997). P occurrence (related to p_0) and magnitude (linked to β) are instead highly and moderately affected by elevation, respectively (Figs. 8, 11-12). These features of STCS and controls on the marginal distribution are also found for winter P when $\Delta t \leq 3$ h. For larger time aggregations, the hypothesis of homogeneous and isotropic STCS is instead less sustained (Fig. 9b), confirming the preliminary analyses of Mascaro (2017; their Fig. 12) who found that directional correlograms of winter P exhibit anisotropic behavior with higher correlations along the northeast–southwest axis. This could be explained by the combined

effect of storm anisotropy, the preferential motion of large-scale frontal storms (as also suggested by Sungmin and Foelsche, 2019), and the orographic barrier of the Mogollon Rim (Fig. 1). The shape of the marginal distribution of P sampled at $\Delta t > 3$ h could still be considered constant (Fig. 9), while elevation is not sufficient to fully explain the spatial variability of P magnitude (Figs. 11-12).

5.2. Generalization of the results and transferability of the approach

The results of this work are consistent with and expand the findings of previous studies. Several efforts (Krajewski et al. 2003; Ciach and Krajewski 2006; Villarini et al. 2008; Sungmin and Foelsche 2019; Peleg et al. 2013) showed that the spatial correlation of high-resolution P

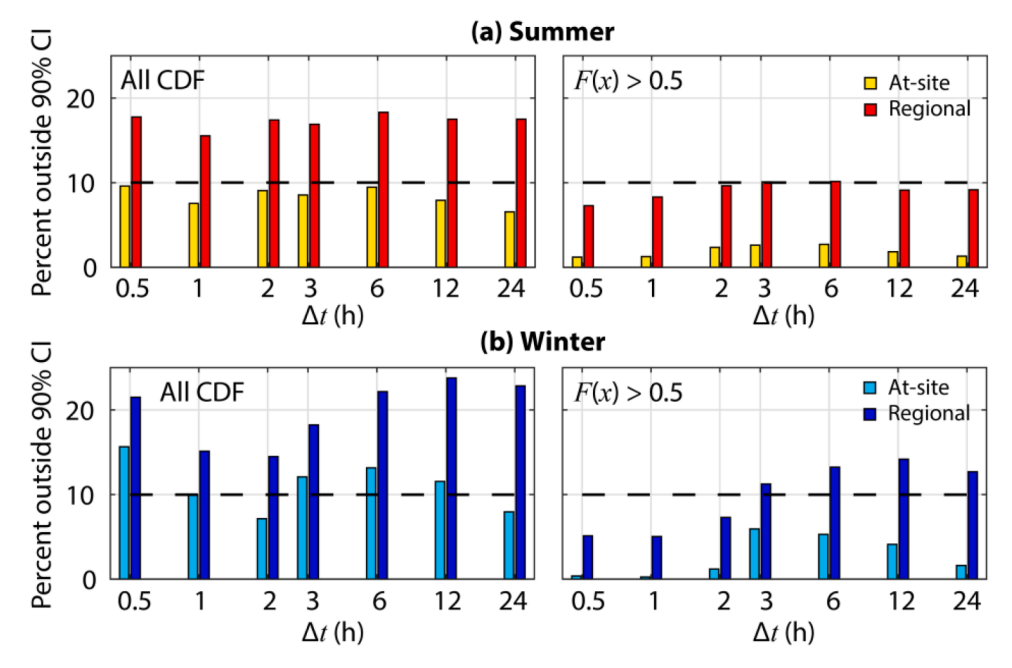


Fig. 12. Mean across the gages of the percent of observed values outside the 90% CI of At-site and Regional simulations considering the entire CDF (left panels) and the portion F(x) > 0.5 (right panels) for (a) summer and (b) winter P.

could decrease significantly within short distances $\delta < \sim 25$ km as P is aggregated at smaller Δt 's, and that the rate of these changes varies with the climatic regimes and seasons. Our findings confirm these outcomes and further expand them by considering larger Δt 's and δ 's thanks to the large spatial coverage and high density of the rain gage network. Our results are also in line with Molnar and Burlando (2008), who showed that winter P in Switzerland, dominated by frontal systems, is more structured (i.e., has higher serial correlation) than summer P resulting from convective storms. This indicates that, qualitatively, the considerations reported in the previous section have general validity at sites with a precipitation regime dominated by convective and frontal systems.

This work provides an effective methodological framework to gain new insights into the space-time P variability at any location, provided that P observations are available with sufficient density and spatial coverage. As known, the most accurate P products are ground observations of dense rain gage networks, which are becoming increasingly available as part of flood warning systems. For example, in the U.S., the counties of Harris, Clark, and Los Angeles, as well as the Santa Clara Valley Water District operate dense rain gage networks to monitor flooding in the metropolitan areas of Houston, Las Vegas, Los Angeles, and San Jose, respectively; dense rain gage networks are also available in Europe (De Vos et al. 2017; O and Foelsche 2019). When rain gages are not available, spatially seamless quantitative precipitation estimates from weather radars (Lin 2011; Zhang et al. 2016), satellite sensors (e.g., Hou et al. 2014), and gridded interpolated products (e.g., NOAA 2021; Kim and Villarini 2022) could be very valuable after their ability to capture marginal distributions and STCS and their overall biases are assessed in regions where dense gage networks are available; this is one of the subjects of our future work. As shown in Fig. 4, the three-parameter distributions cover several combinations of L-moments and, thus, they should be able to capture a large variety of P distribution shapes across climatic regimes; other parametric forms have been proposed by Naveau et al. (2016) and Papalexiou (2022). The Clayton-Copula STCS was found to be a flexible homogeneous and isotropic model that well captures the empirical STCS in our study region. Specifically, the Clayton-Copula STCS has the minimum number of parameters that allow adequate control of the scale and shape of the spatial and temporal correlations (b_S , c_S , b_T , c_T) as well as of their

interactions (θ). If the Clayton-Copula is not considered adequate at other sites, Papalexiou and Serinaldi (2020) and Papalexiou et al. (2021) proposed alternative analytical forms of STCS and provided suggestions to design new analytical models that might be needed to account for anisotropy and/or spatial heterogeneity. Once marginal distribution and STCS have been parameterized, the CoSMoS framework could then be used to validate hypotheses on their variability as done here.

6. Conclusions

This study advances the knowledge of and ability to model the STCS and marginal distribution of short-duration (<24 h) P, two properties that have received relatively little attention in the literature due to the lack of adequate reliable observations. A systematic analysis of the seasonal and spatial variability of these properties is conducted in a large region in central Arizona using a high-density network of gages with long-term, high-resolution P records. The empirical STCSs are captured well by the Clayton-Weibull parametric STCS, while three parametric distributions, namely, the \mathcal{GG} , $\mathcal{B}_{r}XII$, and $\mathcal{GE}4$, describe well the empirical distribution of nonzero P for all Δt 's, with the $\mathcal{GE}4$ providing the best results. These parametric models show that summer P, dominated by short-lived convective thunderstorms, exhibits weaker correlation structure and heavier tails of the distribution than winter P, which is instead controlled by longer and widespread frontal systems. Monte Carlo experiments relying on stochastic simulations with the CoSMoS space-time P model show that, in most cases, the STCS of P could be considered homogeneous and isotropic, the marginal distribution has constant shape across the region, and the spatial variability of P occurrence and mean intensity is controlled by elevation. The only exception is winter P at $\Delta t \geq 3$ h that shows possible non-homogeneity and anisotropy in the STCS and requires additional factors to explain the spatial variability of the mean P intensity.

The methodological framework of this work could be applied at other sites and is then useful for parameterizing, testing, and improving P models and weather generators (Sørup et al. 2016; Paschalis et al. 2013; Peleg et al. 2017; Grimaldi et al. 2022; Kim and Onof 2020), as well as for validating in a statistical sense numerical P simulations from convection-permitting atmospheric models (i.e., verifying the degree to which the probability distributions and space-time correlation

structures of their simulated P time series are consistent with the parametric forms presented here). We identify several future research avenues to further support these goals. The description of the STCS should be improved by accounting for storm advection and anisotropy (Jameson 2021). The potential existence of nonlinear dependencies between the P signals at different time lags should be better quantified and modeled using, e.g., copulas, as recently suggested by Papalexiou (2022). Analyses should also target the characterization of the STCS of the binary signal of rain/no rain, as well as the assessment of the ability of the proposed marginal distributions to capture P extremes and develop strategies to regionalize their parameters. Finally, while the findings of this study did not indicate the existence of significant differences between the STCS and marginal distributions of all nonzero P in urban and non-urban regions of the study area (not shown), additional efforts should be devoted to further investigating the presence of differences by focusing on the extremes, as suggested by the recent study of Huang et al. (2022).

CRediT authorship contribution statement

Giuseppe Mascaro: Conceptualization, Methodology, Software, Validation, Formal analysis, Investigation, Data curation, Writing – original draft, Visualization, Supervision, Funding acquisition. Simon Michael Papalexiou: Conceptualization, Methodology, Software, Writing – original draft, Visualization. Daniel B. Wright: Conceptualization, Writing – original draft.

Declaration of Competing Interest

The authors declare the following financial interests/personal relationships which may be considered as potential competing interests:

Giuseppe Mascaro reports financial support was provided by the National Institute of Standards and Technology and the National Science Foundation

Data availability

Precipitaton data from the FCDMC rain gage network are available at the website https://www.fcd.maricopa.gov/625/Rainfall-Data.

Acknowledgments

We thank three anonymous reviewers for their comments that helped to improve the quality of the paper. This work has been supported by the National Science Foundation (NSF) award #1831475: "SCC: Community-Based Automated Information for Urban Flooding"), and the National Institute of Standards and Technology (NIST) award #70NANB22H056 "Assessing the Utility of Safe-To-Fail Design to Improve Climate Hazards Resilience of Interdependent Infrastructure Systems". The authors thank Stephen D. Waters from the Flood Control District of Maricopa County for providing the rainfall data of the network.

Appendix A. Estimation of distribution parameters using L-moments

Parameters of the \mathscr{GS} , \mathscr{B}_r XII, and \mathscr{GE} 4 were estimated using the numerical procedure proposed by Zaghloul et al. (2020), which is based on the method of L-moments. For distributions with one scale parameter and two shape parameters, the L-variation, τ_2 , and L-skewness, τ_3 , depend only on the shape parameters, τ_1 and τ_2 . Following Hosking (1990), the integral forms of τ_2 and τ_3 are:

$$\tau_2(\gamma_1, \gamma_2) := \frac{\lambda_2}{\lambda_1} = \frac{\int_0^1 Q(u; 1, \gamma_1, \gamma_2) \cdot (2u - 1) du}{\int_0^1 Q(u; 1, \gamma_1, \gamma_2) du}$$
(A1)

$$\tau_3(\gamma_1, \gamma_2) := \frac{\lambda_3}{\lambda_2} = \frac{\int_0^1 Q(u; 1, \gamma_1, \gamma_2) \cdot (6u^2 - 6u + 1) du}{\int_0^1 Q(u; 1, \gamma_1, \gamma_2) \cdot (2u - 1) du},$$
(A2)

where λ_q (q=1,2,3) is the q-order L-moment and $Q(u;1,\gamma_1,\gamma_2)$ is the quantile function of any of the three distributions with scale parameter $\beta=1$. For each record, the sample values of the L-moments, $\hat{\tau}_2$ and $\hat{\tau}_3$, are calculated and parameters γ_1 and γ_2 are estimated by minimizing the squared difference between the sample and theoretical L-moments. In symbols:

$$(\widehat{\gamma}_1, \widehat{\gamma}_2) = \operatorname{argmin}_{(\gamma_1, \gamma_2)} \sum_{1}^{3} \left[\tau_q(\gamma_1, \gamma_2) - \widehat{\tau}_q \right]^2. \tag{A3}$$

Eq. (A3) is solved numerically by substituting Eqs. (A1) and (A2). After estimating γ_1 and γ_2 , the scale parameter β is calculated by minimizing the function:

$$\widehat{\beta} = \operatorname{argmin}_{\beta} [\lambda_1(\beta) - \widehat{\lambda}_1]^2, \tag{A4}$$

where $\lambda_1(\beta)=\int\limits_0^1Q(u;\beta,\gamma_1,\gamma_2)\mathrm{d}u$ and $\widehat{\lambda}_1$ is the sample estimate of the first order L-moment.

Appendix B. Metrics quantifying goodness-of-fit of the parametric distributions

The goodness-of-fit (GOF) of the parametric distributions is quantitatively assessed through the Cramer-von Mises statistic, W^2 (Deidda and Puliga 2006; Laio 2004), and the mean relative mean square error, RelMSE (Papalexiou et al. 2013), defined as:

$$W^{2} = \frac{1}{12n} + \sum_{i=1}^{n} \left[F_{theor}(x_{i}) - F_{emp}(x_{i}) \right]^{2}$$
(A5)

$$ReIMSE = \sum_{i=1}^{n} \left[\frac{F_{theor}(x_i) - F_{emp}(x_i)}{1 - F_{emp}(x_i)} \right]^2,$$
(A6)

where x_i is the *i*-th ascending order statistic, n is the sample size, $F_{theor}(x_i)$ is the theoretical CDFs (one of the three parametric distributions mentioned above), and $F_{emp}(x_i) = \frac{i-0.5}{n}$ is the empirical CDF estimated through the Hazen plotting position formula. Both metrics provide a measure of the correspondence between theoretical and parametric CDFs, with W^2 giving the same weight to all order statistics and RelMSE assigning larger weights to the differences in the right tail of the distribution.

Appendix C. Overview of the Complete Stochastic Modeling Solution (CoSMoS)

We provide here a brief description of the version of CoSMoS used here, referring the reader to Papalexiou (2018) and Papalexiou and Serinaldi (2020) for additional details and to Papalexiou et al. (2021) and Papalexiou (2022) for further developments of this modeling framework. Let $X(s_i, t)$ be a stationary stochastic process describing the time series of P at temporal aggregation Δt at S locations (s_i with i = 1, ..., S). CoSMoS assumes that the process $X(s_i, t)$ can be simulated by transforming a parent standard Gaussian process $Z(s_i, t)$ with an appropriate STCS, $\rho_Z(\tau, \delta)$, related to the STCS of X. The method is applied through the following steps:

- A STCS for X, $\rho_X(\tau, \delta)$, is identified preferably through an analytical model as done in Section 3.2.
- A suitable marginal distribution of P, $F_I(x)$, for X is specified at each gage location.
- The STCS for the parent Gaussian process Z, $\rho_Z(\tau, \delta)$, is obtained by inflating $\rho_X(\tau, \delta)$ through the correlation transformation function:

$$\rho_X(\tau,\delta) = \mathscr{R}(\rho_Z(\tau,\delta)) := \frac{\mathscr{C}(\rho_Z(\tau,\delta)) - \mu_X^2}{\sigma_X},\tag{A7}$$

where μ_X and σ_X are the mean and standard deviation of X, computed from the parametric form of $F_I(x)$, and $\mathscr{C}(\rho_Z(\tau,\delta)) := E(X_IX_j)$ is the expectation of the product between X at two locations i and j. The latter term involves an integral that is solved numerically for a given value of ρ_Z . Therefore, one applies Eq. (A7) to calculate ρ_X for a set of fixed values of ρ_Z (e.g., 0, 0.05, 0.10, ..., 0.95, 1) and then fits an analytical relation to the computed (ρ_Z , ρ_X) pairs to map $\rho_Z \to \rho_X$. Here, the following empirical equation suggested by Papalexiou and Serinaldi (2020) is found to capture well this relation:

$$\rho_{Z} = \frac{\left(1 + b\rho_{X}\right)^{1-c} - 1}{\left(1 + b\right)^{1-c} - 1},\tag{A8}$$

where b and c are coefficients. It is worth noting that, while μ_X and σ_X may vary in space, for this step they could assumed to be constant to simplify the numerical application of CoSMoS with minimal impact of its performance.

• To simulate time series of T time steps at S sites, a multivariate autoregressive model MAR(p) of order p with STCS $\rho_Z(\tau, \delta)$ is used to generate $S \times T$ standard Gaussian variates $z(s_i, t)$. These are transformed into X variates, $x(s_i, t)$, through the marginal back transformation: $x(s_i, t) = F_I^{-1}[\Phi(z(s_i, t))]$, where $\Phi(\cdot)$ is the standard Gaussian CDF. Here, the order p was chosen as the time lag where the serial correlation decays to a negligible value (i.e., 0.05).

References

- Adams, D.K., Comrie, A.C., 1997. The North American monsoon. Bull. Am. Meteorol. Soc. 78, 2197–2213. https://doi.org/10.1175/1520-0477(1997)078<2197:
- Alfieri, L., Thielen, J., 2015. A European precipitation index for extreme rain-storm and flash flood early warning. Meteorol. Appl. 22, 3–13. https://doi.org/10.1002/ MET 1328
- Bárdossy, A., Pegram, G.G.S., 2009. Copula based multisite model for daily precipitation simulation. Hydrol. Earth Syst. Sci. 13, 2299–2314. https://doi.org/10.5194/hess-13-2299-2009.
- Beck, H.E., Zimmermann, N.E., McVicar, T.R., Vergopolan, N., Berg, A., Wood, E.F., 2018. Present and future Köppen-Geiger climate classification maps at 1-km resolution. In: Sci. Data, 5, pp. 1–12. https://doi.org/10.1038/sdata.2018.214. 2018
- Burton, A., Kilsby, C.G., Fowler, H.J., Cowpertwait, P.S.P., O'Connell, P.E., 2008. RainSim: a spatial-temporal stochastic rainfall modelling system. Environ. Modell. Softw. 23, 1356–1369. https://doi.org/10.1016/J.ENVSOFT.2008.04.003. Accessed November 22, 2022.
- Chen, Y., Paschalis, A., Kendon, E., Kim, D., Onof, C., 2021. Changing spatial structure of summer heavy rainfall, using convection-permitting ensemble. Geophys. Res. Lett. 48 https://doi.org/10.1029/2020GL090903 e2020GL090903.
- Ciach, G.J., Krajewski, W.F., 2006. Analysis and modeling of spatial correlation structure in small-scale rainfall in Central Oklahoma. Adv. Water Resour. 29, 1450–1463. https://doi.org/10.1016/j.advwatres.2005.11.003. Accessed May 5, 2021.
- Deidda, R., 2000. Rainfall downscaling in a space-time multifractal framework. Water Resour. Res. 36, 1779–1794. https://doi.org/10.1029/2000WR900038.
- Deidda, R., 2007. An efficient rounding-off rule estimator: application to daily rainfall time series. Water Resour. Res. 43 https://doi.org/10.1029/2006WR005409.

- Deidda, R., Puliga, M., 2006. Sensitivity of goodness-of-fit statistics to rainfall data rounding off. Phys. Chem. Earth 31, 1240–1251. https://doi.org/10.1016/j.pce.2006.04.041. Accessed March 29, 2020.
- Deidda, R., Benzi, R., Siccardi, F., 1999. Multifractal modeling of anomalous scaling laws in rainfall. Water Resour. Res. 35, 1853–1867.
- Deidda, R., Badas, M.G., Piga, E., 2004. Space-time scaling in high-intensity tropical ocean global atmosphere coupled ocean-atmosphere response experiment (TOGA-COARE) storms. Water Resour. Res. 40, 2506. https://doi.org/10.1029/ 2003WR002574
- Emmanouil, S., Langousis, A., Nikolopoulos, E.I., Anagnostou, E.N., 2021. An ERA-5 derived CONUS-wide high-resolution precipitation dataset based on a refined parametric statistical downscaling framework. Water Resour. Res. 57 https://doi. org/10.1029/2020WR029548 e2020WR029548.
- Fowler, H.J., Coauthors, 2021. Anthropogenic intensification of short-duration rainfall extremes. Nat. Rev. Earth Environ. 2, 107–122. https://doi.org/10.1038/s43017-020-00128-6. 2021 2:2.
- Fraedrich, K., Larnder, C., 1993. Scaling regimes of composite rainfall time series. Tellus A: Dynam. Meteorol. Oceanography 45 A, 289–298. https://doi.org/10.3402/ TELLUSA.V4514.14893.
- Gires, A., A. Giangola-Murzyn, J.B. Abbes, I. Tchiguirinskaia, D. Schertzer, and S. Lovejoy, 2014: Impacts of small scale rainfall variability in urban areas: a case study with 1D and 1D/2D hydrological models in a multifractal framework, 12, 607–617, 10.1080/1573062X.2014.923917.
- Grimaldi, S., 2022. Continuous hydrologic modelling for small and ungauged basins: a comparison of eight rainfall models for sub-daily runoff simulations. J. Hydrol. (Amst) 610, 127866. https://doi.org/10.1016/J.JHYDROL.2022.127866. Accessed November 18, 2022.
- Habib, E., Krajewski, W.F., Ciach, G.J., 2001. Estimation of rainfall interstation correlation. J. Hydrometeorol. 2, 621–629. https://doi.org/10.1175/1525-7541 (2001)002<0621:EORIC>2.0.CO;2.

- Harris, D., Foufoula-Georgiou, E., Droegemeier, K.K., Levit, J.J., 2001. Multiscale statistical properties of a high-resolution precipitation forecast. J. Hydrometeorol. 2 https://doi.org/10.1175/1525-7541(2001)002<0406:MSPOAH>2.0.CO;2.
- Hjelmstad, A., A. Shrestha, M. Garcia, and G. Mascaro, 2021: Propagation of radar rainfall uncertainties into urban pluvial flood modeling during the North American monsoon. 10.1080/02626667.2021.1980216, 66, 2232–2248.
- Hosking, J.R.M., 1990. L-Moments: analysis and Estimation of distributions using linear combinations of order statistics. J. R. Stat. Soc. Series B Stat. Methodol. 52, 105–124. https://doi.org/10.1111/J.2517-6161.1990.TB01775.X.
- Hosking, J.R.M., Wallis, J.R., 1997. Regional Frequency Analysis. Cambridge University
 Press
- Hou, A.Y., Coauthors, 2014. The global precipitation measurement mission. Bull. Am. Meteorol. Soc. 95, 701–722. https://doi.org/10.1175/BAMS-D-13-00164.1.
- Huang, J., Fatichi, S., Mascaro, G., Manoli, G., Peleg, N., 2022. Intensification of sub-daily rainfall extremes in a low-rise urban area. Urban Clim. 42 https://doi.org/10.1016/j.uclim.2022.101124.
- Ichiba, A., Gires, A., Tchiguirinskaia, I., Schertzer, D., Bompard, P., ten Veldhuis, M.-C., 2018. Scale effect challenges in urban hydrology highlighted with a distributed hydrological model. Hydrol. Earth Syst. Sci. 22, 331–350. https://doi.org/10.5194/ hess-22-331-2018.
- Jameson, A.R., 2021. On observations of correlation functions and power spectra in rain: obfuscation by advection and sampling. Meteorol. Atmos. Phys. 133 https://doi.org/ 10.1007/s00703-020-00758-x.
- Kim, D., Onof, C., 2020. A stochastic rainfall model that can reproduce important rainfall properties across the timescales from several minutes to a decade. J. Hydrol. (Amst.) 589, 125150. https://doi.org/10.1016/J.JHYDROL.2020.125150. Accessed November 26, 2022.
- Kim, H., Villarini, G., 2022. Evaluation of the analysis of record for calibration (AORC) rainfall across Louisiana. In: Remote Sens. (Basel), 14, p. 3284. https://doi.org/10.3390/RS14143284/S1.
- Krajewski, W.F., Ciach, G.J., Habib, E., 2003. An analysis of small-scale rainfall variability in different climatic regimes. Hydrol. Sci. J. 48, 151–162. https://doi. org/10.1623/hysj.48.2.151.44694.
- Krajewski, W.F., Villarini, G., Smith, J.A., 2010. Radar-rainfall uncertainties:where are we after thirty years of effort. Bull. Am. Meteorol. Soc. 91, 87–94. https://doi.org/ 10.1175/2009BAMS2747.1.
- Laio, F., 2004. Cramer–von Mises and Anderson-Darling goodness of fit tests for extreme value distributions with unknown parameters. Water Resour. Res. 40, 9308. https://doi.org/10.1029/2004WR003204.
- Lewis, E., 2019. GSDR: a global sub-daily rainfall dataset. J. Clim. 32, 4715–4729. https://doi.org/10.1175/JCLI-D-18-0143.1.
- Lin, Y., 2011: GCIP/EOP Surface: precipitation NCEP/EMC 4KM Gridded Data (GRIB) Stage IV Data. Version 1.0.
- Mandapaka, P.V., Qin, X., Mandapaka, P.v., Qin, X., 2015. A large sample investigation of temporal scale-invariance in rainfall over the tropical urban island of Singapore. Theor. Appl. Climatol. 122, 685–697. https://doi.org/10.1007/s00704-014-1317-6. Accessed November 24, 2022.
- Marani, M., 2005. Non-power-law scale properties of rainfall in space and time. Water Resour. Res. 41 https://doi.org/10.1029/2004WR003822.
- Mascaro, G., 2017. Multiscale spatial and temporal statistical properties of rainfall in central arizona. J. Hydrometeorol. 18, 227–245. https://doi.org/10.1175/jhm-D-16-0167.1.
- Mascaro, G., 2018. On the distributions of annual and seasonal daily rainfall extremes in central Arizona and their spatial variability. J. Hydrol. (Amst) 559, 266–281. https://doi.org/10.1016/j.jhydrol.2018.02.011.
- Mascaro, G., 2020. Comparison of local, regional, and scaling models for rainfall intensity-duration-frequency analysis. J. Appl. Meteorol. Climatol. 59, 1519–1536. https://doi.org/10.1175/JAMC-D-20-0094.1
- Mascaro, G., Deidda, R., Hellies, M., 2013a. On the nature of rainfall intermittency as revealed by different metrics and sampling approaches. Hydrol. Earth Syst. Sci. 17 https://doi.org/10.5194/hess-17-355-2013.
- Mascaro, G., Piras, M., Deidda, R., Vivoni, E.R., 2013b. Distributed hydrologic modeling of a sparsely monitored basin in Sardinia, Italy, through hydrometeorological downscaling. Hydrol. Earth Syst. Sci. 17, 4143–4158. https://doi.org/10.5194/hess-17-4143-2013.
- Mascaro, G., Vivoni, E.R., Gochis, D.J., Watts, C.J., Rodriguez, J.C., 2014. Temporal downscaling and statistical analysis of rainfall across a topographic transect in northwest Mexico. J. Appl. Meteorol. Climatol. 53 https://doi.org/10.1175/JAMC D.13.0330 1
- Michaelides, S., Levizzani, V., Anagnostou, E., Bauer, P., Kasparis, T., Lane, J.E., 2009. Precipitation: measurement, remote sensing, climatology and modeling. Atmos. Res. 94, 512–533. https://doi.org/10.1016/J.ATMOSRES.2009.08.017. Accessed November 26, 2022.
- Molnar, P., Burlando, P., 2008. Variability in the scale properties of high-resolution precipitation data in the Alpine climate of Switzerland. Water Resour. Res. 44, 10404. https://doi.org/10.1029/2007WR006142.
- Morbidelli, R., 2020. The history of rainfall data time-resolution in a wide variety of geographical areas. J. Hydrol. (Amst.) 590. https://doi.org/10.1016/j. jhydrol.2020.125258.
- Naveau, P., Huser, R., Ribereau, P., Hannart, A., 2016. Modeling jointly low, moderate, and heavy rainfall intensities without a threshold selection. Water Resour. Res. 52 https://doi.org/10.1002/2015WR018552.
- NOAA Office of Water Prediction, 2021: Analysis of record for calibration version 1.1 sources, methods, and verification.

- O, S., Foelsche, U., 2019. Assessment of spatial uncertainty of heavy rainfall at catchment scale using a dense gauge network. Hydrol. Earth Syst. Sci. 23, 2863–2875. https:// doi.org/10.5194/hess-23-2863-2019.
- Papalexiou, S.M., 2018. Unified theory for stochastic modelling of hydroclimatic processes: preserving marginal distributions, correlation structures, and intermittency. Adv. Water Resour. 115, 234–252. https://doi.org/10.1016/J. ADVWATRES.2018.02.013. Accessed June 25, 2022.
- Papalexiou, S.M., 2022. Rainfall generation revisited: introducing CoSMoS-2s and advancing copula-based intermittent time series modeling. Water Resour. Res. 58 https://doi.org/10.1029/2021WR031641 e2021WR031641.
- Papalexiou, S.M., Koutsoyiannis, D., 2012. Entropy based derivation of probability distributions: a case study to daily rainfall. Adv. Water Resour. https://doi.org/ 10.1016/j.adywatres.2011.11.007.
- Papalexiou, S.M., Koutsoyiannis, D., 2016. A global survey on the seasonal variation of the marginal distribution of daily precipitation. Adv. Water Resour. 94 https://doi. org/10.1016/j.advwatres.2016.05.005.
- Papalexiou, S.M., Serinaldi, F., 2020. Random fields simplified: preserving marginal distributions, correlations, and intermittency, with applications from rainfall to humidity. Water Resour. Res. 56 https://doi.org/10.1029/2019WR026331 e2019WR026331.
- Papalexiou, S.M., Koutsoyiannis, D., Makropoulos, C., 2013. How extreme is extreme? An assessment of daily rainfall distribution tails. Hydrol. Earth Syst. Sci. 17, 851–862. https://doi.org/10.5194/HESS-17-851-2013. Accessed May 11, 2022.
- Papalexiou, S.M., Serinaldi, F., Porcu, E., 2021. Advancing space-time simulation of random fields: from storms to cyclones and beyond. Water Resour. Res. https://doi. org/10.1029/2020WR029466 e2020WR029466.
- Paschalis, A., Molnar, P., Fatichi, S., Burlando, P., 2013. A stochastic model for high-resolution space-time precipitation simulation. Water Resour. Res. 49, 8400–8417. https://doi.org/10.1002/2013WR014437.
- Paschalis, A., Fatichi, S., Molnar, P., Rimkus, S., Burlando, P., 2014. On the effects of small scale space–time variability of rainfall on basin flood response. J. Hydrol. (Amst) 514, 313–327. https://doi.org/10.1016/J.JHYDROL.2014.04.014. Accessed November 21, 2022.
- Peleg, N., Ben-Asher, M., Morin, E., 2013. Radar subpixel-scale rainfall variability and uncertainty: lessons learned from observations of a dense rain-gauge network. Hydrol. Earth Syst. Sci. 17, 2195–2208. https://doi.org/10.5194/HESS-17-2195-2013. Accessed November 20, 2022.
- Peleg, N., Fatichi, S., Paschalis, A., Molnar, P., Burlando, P., 2017. An advanced stochastic weather generator for simulating 2-D high-resolution climate variables. J. Adv. Model. Earth Syst. 9, 1595–1627. https://doi.org/10.1002/2016MS000854.
- Piras, M., Mascaro, G., Deidda, R., Vivoni, E.R., 2014. Quantification of hydrologic impacts of climate change in a Mediterranean basin in Sardinia, Italy, through highresolution simulations. Hydrol. Earth Syst. Sci. 18 https://doi.org/10.5194/hess-18-5201-2014
- Prein, A.F., Liu, C., Ikeda, K., Trier, S.B., Rasmussen, R.M., Holland, G.J., Clark, M.P., 2017a. Increased rainfall volume from future convective storms in the US. Nat. Clim. Change 7, 880–884. https://doi.org/10.1038/s41558-017-0007-7.
- Prein, A.F., Rasmussen, R.M., Ikeda, K., Liu, C., Clark, M.P., Holland, G.J., 2017b. The future intensification of hourly precipitation extremes. Nat. Clim. Change 7, 48–52. https://doi.org/10.1038/nclimate3168.
- Rebora, N., Ferraris, L., von Hardenberg, J., Provenzale, A., 2006. RainFARM: rainfall downscaling by a filtered autoregressive model. J. Hydrometeorol. 7 https://doi. org/10.1175/JHM517.1.
- Schertzer, D., Lovejoy, S., 1987. Physical modeling and analysis of rain and clouds by anisotropic scaling multiplicative processes. J. Geophys. Res. 92, 9693. https://doi. org/10.1029/JD092iD08p09693.
- Schleiss, M., Jaffrain, J., Berne, A., 2011. Statistical analysis of rainfall intermittency at small spatial and temporal scales. Geophys. Res. Lett. 38 https://doi.org/10.1029/ 2011GL049000.
- Seo, D., Lakhankar, T., Mejia, J., Cosgrove, B., Khanbilvardi, R., 2013. Evaluation of operational national weather service gridded flash flood guidance over the arkansas red river basin. JAWRA J. Am. Water Resour. Assoc. 49, 1296–1307. https://doi. org/10.1111/jawr.12087.
- Sørup, H.J.D., Christensen, O.B., Arnbjerg-Nielsen, K., Mikkelsen, P.S., 2016. Downscaling future precipitation extremes to urban hydrology scales using a spatio-temporal Neyman–Scott weather generator. Hydrol. Earth Syst. Sci. 20, 1387–1403. https://doi.org/10.5194/hess-20-1387-2016.
- Sungmin, O., Foelsche, U., 2019. Assessment of spatial uncertainty of heavy rainfall at catchment scale using a dense gauge network. Hydrol. Earth Syst. Sci. 23, 2863–2875. https://doi.org/10.5194/HESS-23-2863-2019. Accessed November 26, 2022.
- Tang, G., Ma, Y., Long, D., Zhong, L., Hong, Y., 2016. Evaluation of GPM Day-1 IMERG and TMPA Version-7 legacy products over Mainland China at multiple spatiotemporal scales. J Hydrol (Amst) 533, 152–167. https://doi.org/10.1016/J. JHYDROL.2015.12.008. Accessed November 21, 2022.
- Veneziano, D., Langousis, A., 2005. The areal reduction factor: a multifractal analysis. Water Resour. Res. 41, 1–15. https://doi.org/10.1029/2004WR003765. Accessed November 25, 2022.
- Venugopal, V., Foufoula-Georgiou, E., Sapozhnikov, V., 1999. A space-time downscaling model for rainfall. J. Geophys. Res. Atmos. 104, 19705–19721. https://doi.org/ 10.1029/1999JD900338.
- Verrier, S., Mallet, C., Barthès, L., 2011. Multiscaling properties of rain in the time domain, taking into account rain support biases. J. Geophys. Res. Atmos. 116, 20119. https://doi.org/10.1029/2011JD015719.

- Villarini, G., Mandapaka, P.v., Krajewski, W.F., Moore, R.J., 2008. Rainfall and sampling uncertainties: a rain gauge perspective. J. Geophys. Res. Atmos. 113, 11102. https:// doi.org/10.1029/2007JD009214.
- De Vos, L., Leijnse, H., Overeem, A., Uijlenhoet, R., 2017. The potential of urban rainfall monitoring with crowdsourced automatic weather stations in Amsterdam. Hydrol. Earth Syst. Sci. 21, 765–777. https://doi.org/10.5194/HESS-21-765-2017. Accessed March 26, 2023.
- Wright, D.B., Asce, M., Smith, J.A., Baeck, M.L., 2013. Critical examination of area reduction factors. J. Hydrol. Eng. 19, 769–776. https://doi.org/10.1061/(ASCE) HE.1943-5584.0000855.
- Wright, D.B., Smith, J.A., Baeck, M.L., 2014. Flood frequency analysis using radar rainfall fields and stochastic storm transposition. Water Resour. Res. 50, 1592–1615. https://doi.org/10.1002/2013WR014224.
- Zaghloul, M., Papalexiou, S.M., Elshorbagy, A., Coulibaly, P., 2020. Revisiting flood peak distributions: a pan-Canadian investigation. Adv. Water Resour. 145, 103720 https://doi.org/10.1016/J.ADVWATRES.2020.103720. Accessed November 29, 2021.
- Zawadzki, I.I., 1973. Statistical properties of precipitation patterns. J. Appl. Meteorol. 12 https://doi.org/10.1175/1520-0450(1973)012<0459:spopp>2.0.co;2.
- Zhang, J., Coauthors, 2016. Multi-Radar Multi-Sensor (MRMS) quantitative precipitation estimation: initial operating capabilities. Bull. Am. Meteorol. Soc. 97, 621–638. https://doi.org/10.1175/BAMS-D-14-00174.1.